Petroleum Science 20 (2023) 2726–2746

Contents lists available at ScienceDirect

Petroleum Science

journal homepage: www.keaipublishing.com/en/journals/petroleum-science

Original Paper

Microscopic oil occurrence in high-maturity lacustrine shales: Qingshankou Formation, Gulong Sag, Songliao Basin

Jing-Ya Zhang*, Ru-Kai Zhu**, Song-Tao Wu, Xiao-Hua Jiang, Chang Liu, Yi Cai, Su-Rong Zhang, Tian-Shu Zhang

Research Institute of Petroleum Exploration and Development, PetroChina, Beijing, 100083, China

ARTICLE INFO

Article history:
Received 14 December 2022
Received in revised form
27 July 2023
Accepted 21 August 2023
Available online 22 August 2023

Edited by Jie Hao and Teng Zhu

Keywords:
Shale oil content
Occurrence states
Micro-oil distribution
Effective pore spaces
Controlling factors
Gulong sag

ABSTRACT

Occurrence and mobility of shale oil are prerequisites for evaluating shale oil reserves and prioritizing exploration targets, particularly for heterogeneous lacustrine shales. The Qingshankou Formation in the Gulong Sag, Songliao Basin is a classic lacustrine pure shale reservoir that contains abundant shale oil resources. The predicted geological reserves of the shale are 1.268×10^9 t. In this study, field emission scanning electron microscope (FE-SEM), the modular automated processing system (MAPS), pyrolysis-gas chromatography (Py-GC), low-pressure nitrogen gas adsorption (LPNA), Soxhlet extraction, pyrolysis, and 2-D nuclear magnetic resonance (NMR) were integrated to describe the shale oil components, microscopic occurrence, mobility, and the effective pore size distribution. Meanwhile, the related controlling factors are discussed.

The shale oil in the Qingshankou Fm exists dominantly in the matrix pores of the clay minerals, with small amounts distributed in the intergranular pores of terrigenous clastic grains, intercrystalline pores of pyrite, intragranular pores of ostracod shells, and micro-fractures. Shale oil is distributed in the pore spaces of variable sizes in different lithofacies. The clay mineral-laminated shales are characterized by the broadest range of pore size and largest volume of pore spaces with shale oil distribution, while the ostracod-laminated shales have limited pore spaces retaining oil. Furthermore, the proposed integrated analysis evaluates the shale oil molecules existing in two states: movable, and adsorbed oil, respectively. The result illustrates that movable oil takes up 30.6%–79.4% of the total residual oil. TOC, mineral composition, and pore structures of the shale joint together to control the states and mobility of the shale oil. TOC values are positively correlated with the quantities of shale oil regardless of the state of oil. The mineral components significantly impact the state of shale oil. Noticeable differences in the states of oil were observed following the changing types of minerals, possibly due to their difference in adsorption capacity and wettability. Clay minerals attract more adsorbed oil than movable oil. Felsic minerals generally decrease the occurrence of total and adsorbed oil. Carbonate plays a positive role in hydrocarbon retention of all the shale oil states. As for the pore structure, the average pore size exerts a critical impact on the total, movable, and adsorbed oil content. The total pore volume and specific surface area of shales play a principal role in controlling the total yields and amounts of adsorbed oil. This research improves the understanding of the occurrence characteristics and enrichment mechanisms of shale oil in terrestrial pure shales and provides a reference for locating favorable shale oil exploration areas.

1. Introduction

Shale oil systems consist of organic-rich shale/mudstone units where a significant portion of generated oil is retained in situ. The initial exploration breakthrough of shale oil resources in the U.S. was achieved in 1953 by a vertical well drilled into the Bakken Formation (Tran et al., 2011). Following the technical development

* Corresponding author.
** Corresponding author.
E-mail addresses: zhangjingya@petrochina.com.cn (J.-Y. Zhang), zrk@petrochina.com.cn (R.-K. Zhu).

https://doi.org/10.1016/j.petsci.2023.08.026

of horizontal drilling and hydraulic fracturing, shale oil production increased dramatically and blossomed between 2005 and 2010 (Han et al., 2015; Soeder, 2018). The U.S. produced 3.6×10^8 tons of shale oil in 2020, contributing to 65% of the total oil production (EIA, 2021). In contrast to the successfully played and commercialized marine shale in the U.S., the exploration of lacustrine shale oil in China is still at its preliminary stage with various challenges upfront. Compared with the marine shale plays in North America, the geological conditions of the terrestrial shale oil in China are more complicated, characterized by heterogenous lithofacies, unstable reservoir distribution, low oil maturity, high clay content, and relatively low organic matter (OM) abundance (Katz and Lin, 2014; Liu et al., 2019; Wu et al., 2019; Liu et al., 2020a). In recent years, China has made unprecedented breakthroughs in the lacustrine shale oil exploration and development in a variety of places, including the Junggar basin, Ordos Basin, Santanghu Basin, Songliao Basin, Bohai Bay Basin, and Qaidam Basin (Liu et al., 2019; Liu et al., 2020a; Zhao et al., 2020; Hu et al., 2021; Liu et al., 2021b; Sun et al., 2021; Zhu et al., 2021), indicating the existence of sizeable potential oil resources in the lacustrine shales.

In 2021, a significant shale oil discovery was made in the Qingshankou Formation of the Gulong Sag, Songliao Basin, with a predicted geological reserve of 1.268×10^9 t (Jin et al., 2022). Several horizontal wells completed in the Qingshankou Formation shale, including GY1H, YY1H, and GY2HC, tested stable oil flow over 30 m^3/d (Jin et al., 2022). Well-GYP1 has produced oil continuously over 480 days with a commercial oil production rate of 30.5 t/d and a gas production rate of 13,032 m^3/d (Sun et al., 2021). The successful exploration and exploitation of shale oil in the Gulong Sag marked the shale oil revolution of China, even worldwide. It is the first time China received industrial oil production from pure shale formations, which is totally different from the successfully played shale oil in the U.S., whose shale oil production mainly came from the oil in the tight sandstone or carbonate reservoirs interbedded with marine shales (Jarvie, 2012; Han et al., 2019). In previous exploration domestically and abroad, organic-rich mudstones and shales commonly act as both the source of hydrocarbon and reservoir, but the optimum production was mainly from the associated organic-lean juxtaposed carbonates, silts, or sands in the shale-oil resource system (Jarvie, 2012). In contrast, the commercial production of oil in pure shales, such as the Qingshankou shale oil in the Gulong Sag, changed the conventional view and revealed great resource potential in terrestrial shale oil.

Liquid oil exists primarily in two forms in the organic-rich shales: free oil and adsorbed-miscible oil. The free oil in the nano-micrometer scale pore spaces and fractures is often considered as movable oil. The adsorbed-miscible oil exists in the interior of kerogen or on the surface of hydrophobic kerogen/mineral particles (Sang et al., 2018b; Li et al., 2020a; Guan et al., 2022), which is commonly treated as immovable oil. Actually, the shale oil production capacity is mainly determined by the amount of free oil. Therefore, quantifying the free-to-total oil ratio is crucial for exploring shale oil potential "sweet spots" and evaluating available resources. Previous studies indicate that the Qingshankou shale in the Gulong Sag has a favorable organic matter type (mainly lamalginite), high maturity, and excellent oil-bearing property (Liu et al., 2019). However, one of the most critical issues remain poorly investigated is the shale oil occurrence characteristics and its mobility. Knowledge of the shale oil amount, microscopic occurrence characteristics, and effective pore spaces are essential to the study of pore-scale oil distribution in shale reservoirs, and to further investigate the controlling factors of the states of shale oil, both of which are prerequisites for evaluating shale oil reserves and optimizing promising exploration targets.

Numerous researchers have established systematic methods to quantitatively evaluate the states and mobility of shale oil, including the oil saturation test from cores (Jarvie, 2012, Jarvie, 2014; Cao et al., 2017), multiple isothermal stages pyrolysis (MISP) (Jiang et al., 2016; Abrams et al., 2017; Romero-Sarmiento, 2019), sequential solvent extraction (SSE) (Gorynski et al., 2019; Zhang et al., 2019; Liu et al., 2020a), low frequency (2 MHz) nuclear magnetic resonance (NMR) measurement combined with centrifugation or other displacement experiments (Karimi et al., 2015; Jiang et al., 2021), molecular dynamics simulation method (Wang et al., 2016; Tian et al., 2017), and swelling method (Hruljova et al., 2013; Huang et al., 2020). However, most of these experiments are complicated, time-consuming, and expensive. In particular, the current commonly applied MISP and SSE methods need adjustments in the thermal interval during pyrolysis, sample particle size, types of solvent, and time of heating or extraction, all of which can affect shale oil occurrence and mobility evaluation results. Recently a non-destructive technique, high frequency (HF, 19 MHz) multidimensional NMR, has been widely used to characterize the mobility of fluids in tight sandstone and shale reservoirs. HF NMR has 30–50 fold more sensitivity than low frequency (LF) NMR to identify hydrogen signals from different proton populations, which is an ideal tool to distinguish the coexisting hydroxyl groups (OH), solid organic matter (OM), as well as oil/bitumen and water in the pores and fractures of shale oil reservoirs (Fleury and Romero-Sarmiento, 2016; Mehana and El-monier, 2016; Khatibi et al., 2019; Li et al., 2020a; Liu et al., 2021a). Therefore, it offers a better resolution to demonstrate the existing states of the shale oil and percentage of the movable oil combined with other methods (Nicot et al., 2016; Li et al., 2020b).

In this study, we use samples from the shale reservoir in the Qingshankou Formation, Gulong Sag, to illustrate the microscopic occurrence characteristics and mobility of the new type of shale oil yielded in the highly mature pure terrestrial shales. At first, the shale oil component was depicted by the integrated measurements of the physical property of the crude oil, group component analysis, and pyrolysis-gas chromatography. Then, the shale oil occurrence characteristics and effective pore size distribution were investigated systematically by the comprehensive characterization of SEM observation, MAPS statistics, and comparison of LPNA before and after Soxhlet extraction. Next, the shale oil in different states (total residual, movable, and adsorbed oil) were identified and quantitatively evaluated by combining Soxhlet extraction, pyrolysis, and 2-D NMR. Finally, the controlling factors on shale oil amounts, states, and mobility were discussed. This study improves the understanding of enrichment mechanisms and controlling factors of the highly mature terrestrial shale oil in pure shale formations, guiding the exploration and development of the "sweet spots" of shale oil.

2. Geological setting

The Songliao Basin, located in northeastern China (Fig. 1a), is one of the largest oil- and gas-prone sedimentary basins worldwide. Based on the basement characteristics and tectonic evolution, the basin is divided into six first-order tectonic units, including Western Slope, Northern Plunge, Northeastern Uplift, Southeastern Uplift, Southwestern Uplift, and Central Depression (Fig. 1b). The studied Gulong Sag is located in the Central Depression, with an area of 3000 km^2. The stratigraphy in the Gulong Sag consists of the Cretaceous, Paleogene, Neogene, and Quaternary sequences with a maximum total thickness of 10 km. The interval of interest is the upper Cretaceous Qingshankou Formation (Fig. 1c), one of the critical shale oil layers and the best source rocks in the Songliao

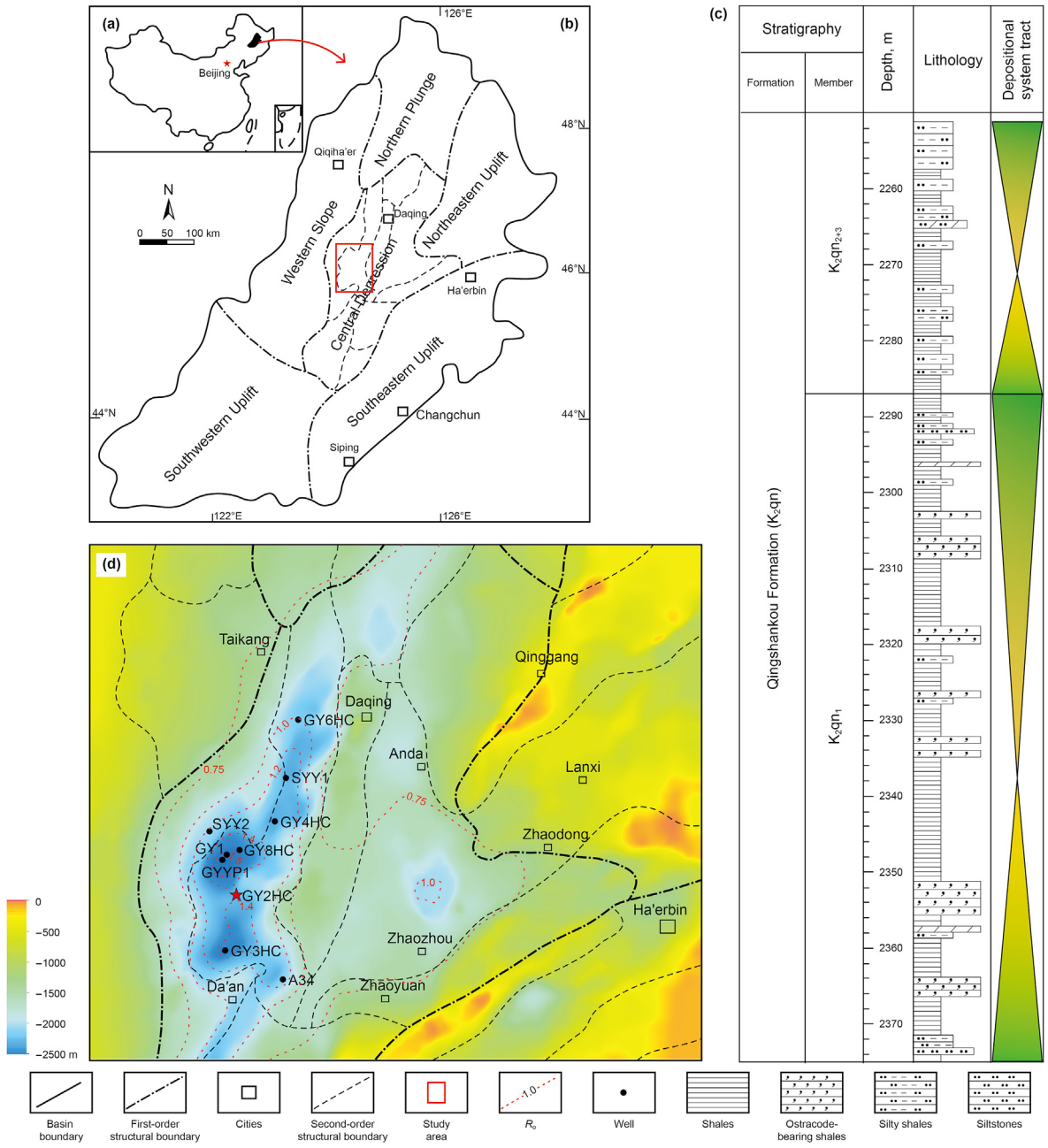

Fig. 1. Location map (a) and sketch map (b) of the six first-order tectonic units in the Songliao Basin (modified after Zhang et al., 2020a. (c) General stratigraphic column of the Qingshankou Fm, Gulong Sag. (d) Well locations in the study area (modified after Sun et al., 2021).

Basin. The Qingshankou Formation (K_2qn) deposited in a deep to semi-deep lake is subdivided into three members. During the deposition of the first member (K_2qn_1), the lake basin experienced a complete transgressive-regressive sedimentary cycle and formed a set of black or dark organic matter-rich laminated shales (Fig. 1c). During the deposition of the second and third member (K_2qn_{2+3}), the lake basin shrunk followed by more terrigenous clastic supply. Afterward, more silts were developed.

The lithofacies of the Qingshankou shales in the Gulong Sag were divided into four types based on the laminae types, including felsic-laminated shales (FLS) (Fig. 2a–d), ostracod-laminated shales (OLS) (Fig. 2e–h), clay mineral-laminated shales (CLS) (Fig. 2i and j), and mixed-laminated shale (MLS). MLS is defined as it contains a mixture of clay mineral-, felsic-, and ostracod-laminae (Fig. 2k–l). The XRD data show that the mineral compositions and their percentages in the shales of the Qingshankou Fm are clay minerals at 44.1%–63.1%, averaging 3.3%, quartz at 26%–35.1%, averaging 30.2%, and plagioclase at 5.0%–10.8%, averaging 7.3% respectively. Additionally, the shale contains 3.6% calcite, 3.1% pyrite, 1.6% ankerite, and 0.9% feldspar. Clay mineral content higher than 50% is commonly observed in the shales of the Qingshankou Fm in the Gulong Sag, which is different from most shale oil reservoirs domestically and abroad. The predominant types of clay minerals include illite (I), illite/smectite mixed layer (I/S), and chlorite (C), which averagely take up 72%, 16%, and 12% of the total, respectively.

Most shale samples in the Qingshankou Formation show a characteristic of high organic matter abundance. The TOC ranges from 1.31 to 4.26 w. t.%, with an average of 2.69 w. t.%. The pyrolysis

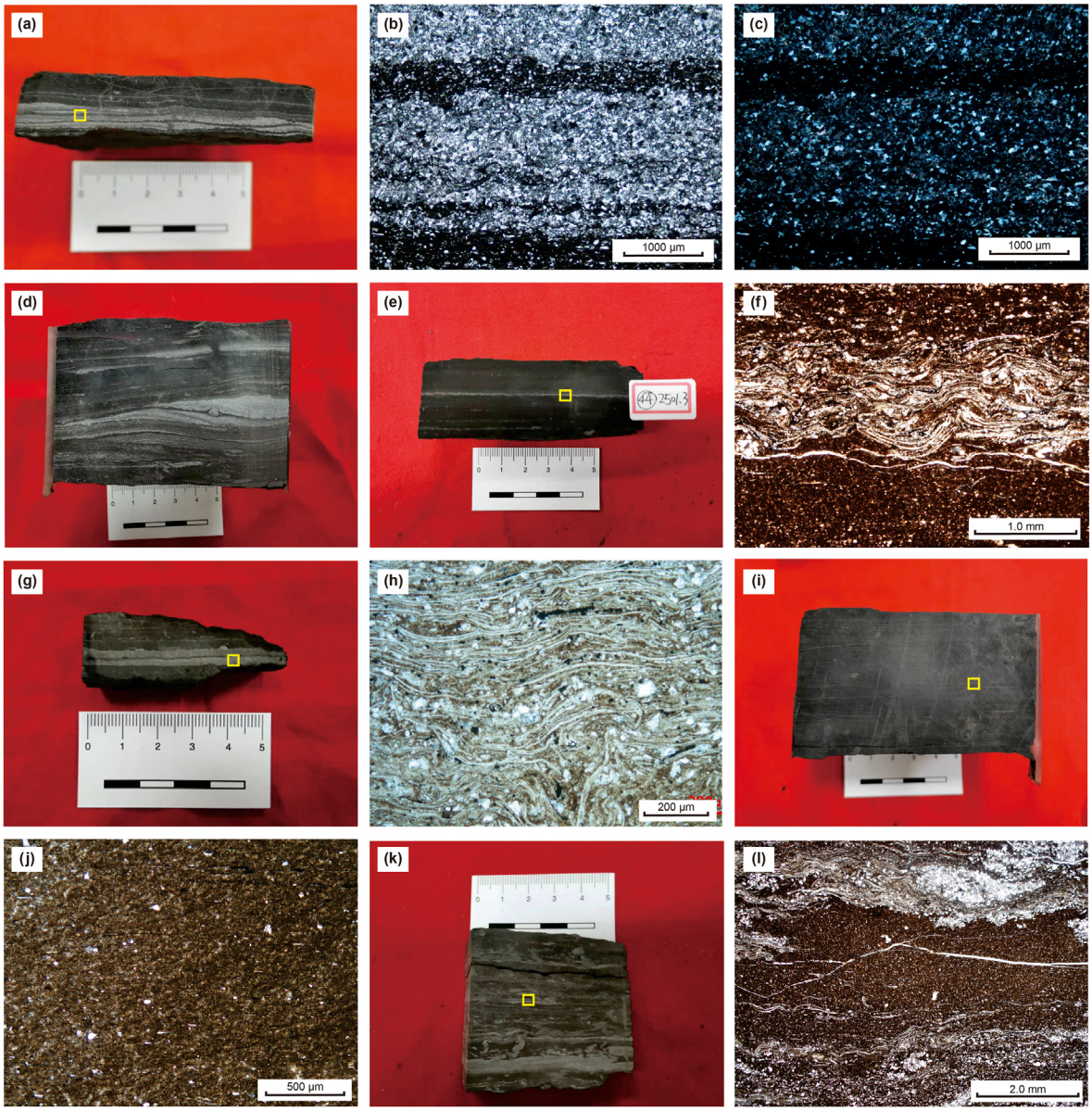

Fig. 2. Petrological characteristics of the main lithofacies of shales in the Qingshankou Fm, Gulong Sag. (PPL = plane-polarized light; CPL = cross-polarized light) (a) Felsic-laminated shale, GY8HC, 2461.6 m; (b) The felsic laminae in shales, zoom in view of the yellow box in (a), PPL; (c) The felsic laminae in shales, same as (b), CPL; (d) Felsic-laminated shale, GY8HC, 2409.1 m; (e) Ostracod-laminated shale, GY3HC, 2501.3 m; (f) The ostracod laminae in shale, zoom in view of the yellow box in (e), PPL; (g) Ostracod-laminated shale, GY8HC, 2474.64 m; (h) zoom in view of the yellow box in (g), PPL; (i) Clay mineral-laminated shale, GY8HC, 2493.1 m; (j) Magnified part of the yellow box in (i), PPL; (k) Mixed-laminated shale, GY3HC, 2455.3 m; (l) mixed sedimentation of felsic minerals and ostracod components, zoom in view of the yellow box in (k), PPL.

result illustrates that the S_1 values are between 1.81 and 8.1 mg/g, averaging 3.84 mg/g. The S_2 values are between 1.47 and 7.30 mg/g, averaging 3.69 mg/g. The hydrocarbon generation potential (HI, calculated as S_2/TOC) is between 94.8 and 171.5 mg/g, with an average value of 135.3 mg/g. The kerogen type is dominantly type I and type II. Furthermore, R_o in the range of 1.15–1.41%, averaging 1.29%, and T_{max} in the range of 434–474 °C, averaging 454 °C, indicate high maturity in the organic matter of K_2qn_1.

3. Samples and methods

For the experiments, a series of samples of Qingshankou Fm. Shales was retrieved from Well GY2HC, GY3HC, and GY8HC in the Gulong Sag, northern Songliao Basin (Fig. 1d). We apply the integrated methods to characterize the shale oil content at different states of occurrence and investigate the microscopic occurrence characteristics and effective pore spaces of shale oil. Laboratory tests, including Soxhlet extraction, TOC content measurements, Rock-Eval pyrolysis, XRD analysis, and LPNA, were performed on 19 shale samples. Based on the results from these measurements, 11 shale samples with significant differences in pyrolysis parameters were selected for 2D NMR. Two typical samples with high oil content were selected for MAPS and Py-GC analysis.

3.1. Soxhlet extraction, TOC, and Rock-Eval pyrolysis

The core samples were pulverized into 200 meshes after cleaning their surface. Then Soxhlet extraction was conducted on the rock powders using dichloromethane for 72 h until no fluorescence was observed. The TOC content was measured using the

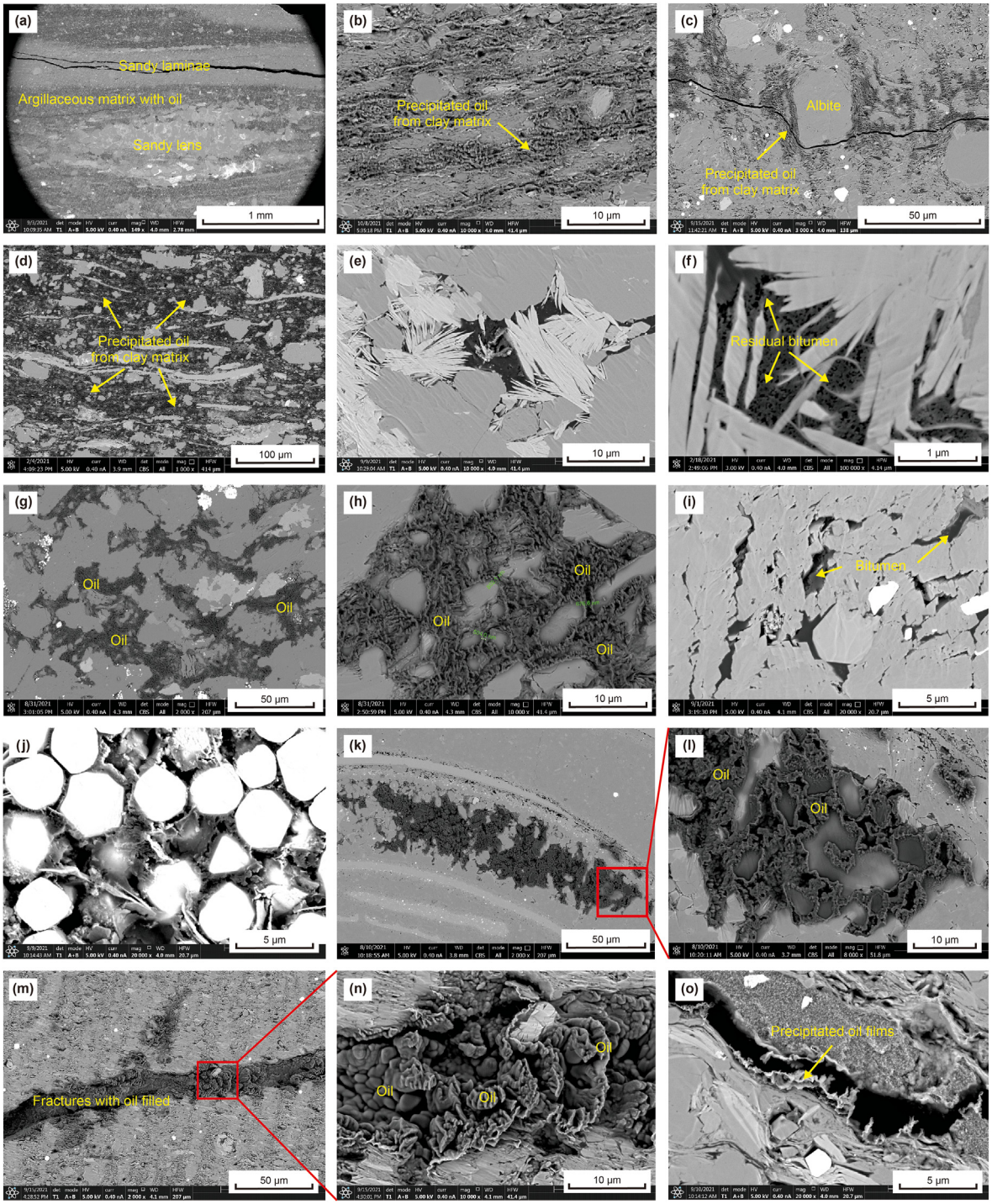

Fig. 3. Characteristics of oil in shales. (a) Oil mainly distributed in argillaceous matrix but barely existed in strongly cemented sandy lens or laminae, GY8HC, 2505.1 m; (b) Precipitated oil from clay mineral laminae, GY8HC, 2511.1 m; (c) Precipitated oil from clay mineral matrix, GY8HC, 2421.1 m; (d) Precipitated oil from clay mineral matrix, GY2HC, 2352.9 m; (e) Residual bitumen in the intercrystalline pores of clay minerals, GY3HC, 2490.6 m; (f) Organic pores developing in the residual bitumen in the intercrystalline pores of clay minerals, GY1, 2551.6 m; (g) Precipitated oil in the intergranular pores of clastic grains, GY3HC, 2497.25 m; (h) Precipitated oil in the intergranular pores of clastic grains, GY3HC, 2497.25 m; (i) Residual bitumen in the intergranular pores of clastic grains, GY3HC, 2490.6 m; (j) Precipitated oil in pyrite intercrystalline pores, GY8HC, 2458.2 m; (k) Precipitated oil in the intragranular pores of ostracods GY3HC, 2511.65 m; (l) The enlarged part of the red box in (k), GY3HC, 2511.65 m; (m) Oil filled in the micro-fractures of shales, GY8HC, 2484.1 m; (n) The enlarged part of the red box in (m), GY8HC, 2484.2 m; (o) Precipitated oil films attached to the edges of a micro-fracture, GY8HC, 2429.0 m.

eltraCS-I instrument. Pyrolysis analysis was performed on the original unextracted and post-solvent extracted core powders using Rock-Eval 6 device. The details of the experimental procedure were illustrated by Abrams et al. (2017).

3.2. Nuclear magnetic resonance (NMR) relaxometry

Multidimensional NMR techniques improve the separation of the different proton contributions. The two-dimensional NMR mapping techniques provide better differentiation when plotting

both T_1 and T_2 relaxations time simultaneously. The 2-D NMR quantitative analysis was conducted on 11 samples, carried out on MesoMR23-040 V low-field NMR analyzer instrument with a proton Larmor frequency of 19.45 MHz and a magnetic field intensity of 0.46 T (manufactured by Suzhou Niumag Company Ltd). All measured samples were shale blocks with various shapes ranging from 10 g to 18 g in weight. NMR T_1-T_2 correlation data were acquired using a pulse sequence combining T_1 and T_2 data acquisitions. A saturation recovery sequence was followed by a Carr-Purcell-Meiboom-Gill (CPMG) sequence, where 31 T_1 wait steps were used, and 3000 echoes were recorded at each T_1 step. The echo time spacing (TE) was 0.08 ms, and the T_1 weighted delays were from 0.058 ms to 2 s with 31 steps by equal logarithm interval. The inversion of 2D NMR data was processed using the improved Butler-Reeds-Dawson (BRD) algorithm to obtain a 2D T_1-T_2 map (Butler et al., 1981; Liu et al., 2020b).

3.3. Thin section and field emission-scanning electron microscope (FE-SEM)

The core blocks were mechanically polished in a direction perpendicular to the lamina. Thin sections were analyzed under transmitted white light using a Leica DM4500 microscope with LED illumination and a LAS V4.2 digital camera detection system. The sample blocks prepared for FE-SEM analysis were mechanically polished on the surface and then polished by argon ion using a Leica EM RES102 Ion Beam Milling System. The experiment was then conducted using an FEI Helios Nano-Lab 650 FE-SEM after the polished surface was coated with carbon. The accelerating voltage, current and working distance were 5 kV, 0.4 nA, and 4.0 mm, respectively. EDS energy spectrum analysis was performed on a Bruker (Czechoslovakia) energy spectrometer with a working voltage, current, and distance of 20 kV, 1.6 nA, and 4.0 mm, respectively.

3.4. X-ray diffraction

The mineral components of shales were analyzed utilizing a Bruker D2 PHASER X-ray diffraction instrument, with the emissive and receiving slits of 0.6 mm and 8 mm, respectively. A Cu-target Ceramic X-ray tube was equipped with the diffractometer, and the samples were scanned from 6° to 55° with a step size of 0.02° (2θ). The mineral composition was quantified using Jade 6 software in conjunction with Rochquan+2012 software developed by the Research Institute of Petroleum Exploration and Development of PetroChina Company (Zhang et al., 2020a).

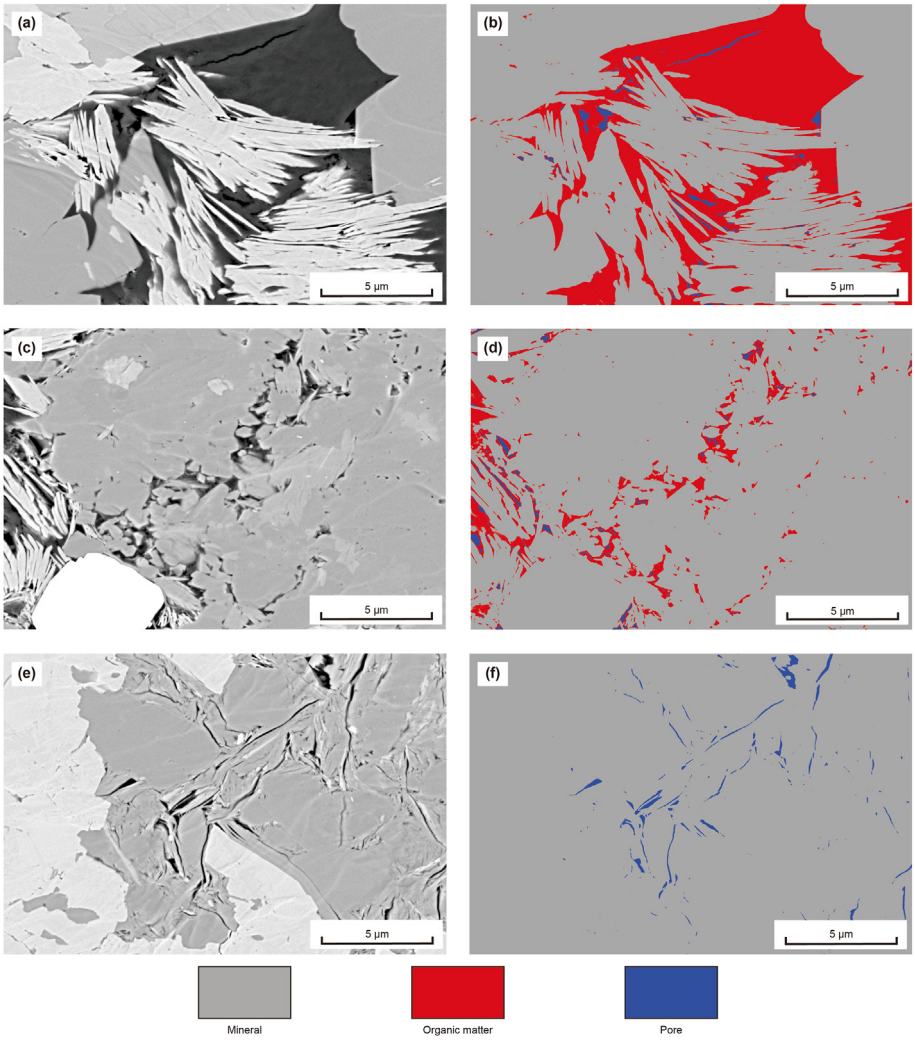

Fig. 4. Images of automated MAPS measurement of the Qingshankou shales. The images are divided into three types, shales with chunks of solid OM (Type I, a), shales with residual oil (Type II, c), and shales with no residual oil or OM (Type III, e). The images of b, d, and f are the segmented images of a, c, and e, respectively. The segmented components include minerals (marked as grey color), organic matter (marked as red color), and pore spaces (marked as blue color).

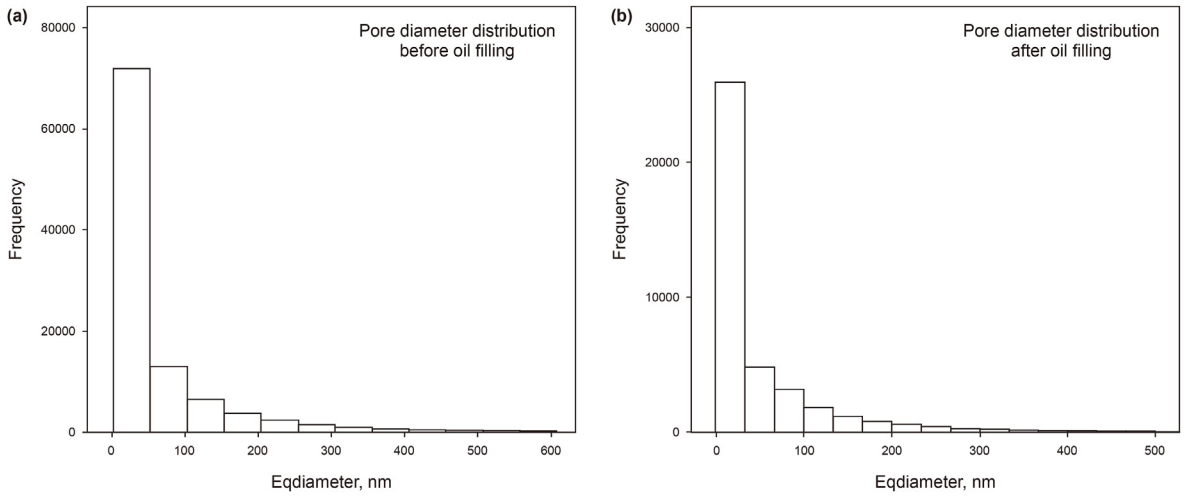

Fig. 5. The pore size distribution before and after oil accumulation depicts the oil film thickness in the pore spaces in the Qingshankou shales.

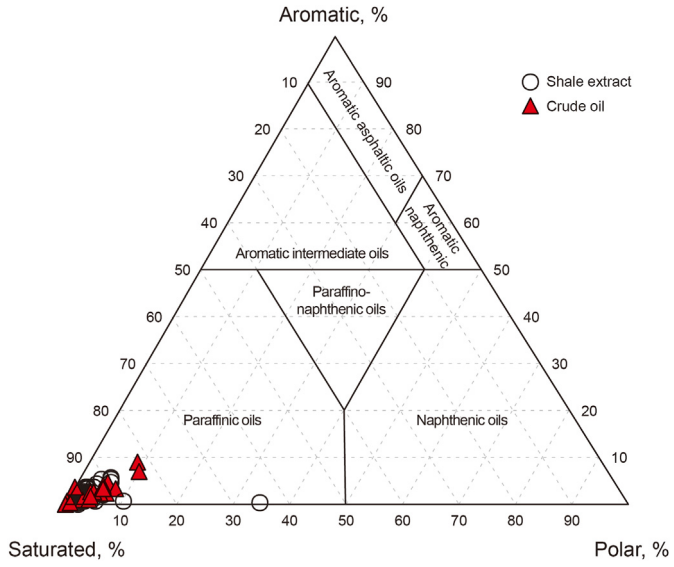

Fig. 6. Ternary diagrams on the potential petroleum class generated from the bitumen composition of shale samples and crude oil.

3.5. The modular automated processing system (MAPS)

MAPS software was applied for the high-resolution large-format SEM images automatically acquired by Thermo Scientific™ Apreo SEM. The surface area of interest was divided into a grid format with 35 × 40 tiles. A sequence of BSE images was acquired in real-time with a 15% overlap, then subsequently merged to generate one single image. Images of 59,691 × 59,188 pixels for the shale sample with a pixel size of 10 nm were captured at an energy of 5 keV, 0.4 nA, and an acquisition time of 8 μs per pixel. The final mosaic of images allows for systematically investigating the microscopic occurrence of shale oil from the nm- to mm- scales.

3.6. Low-pressure nitrogen gas adsorption (LPNA)

Nitrogen gas adsorption is a powerful method that accurately determines the amount of gas adsorbed on solid materials and then directly estimates the porosity and pore structure of materials (Schmitt et al., 2013). Before loading for the LPNA test, shale samples were crushed and sieved into 60–80 mesh size (180–250 μm) fragments to preserve the entire shale microstructures. Then, the samples were degassed for at least 8 h at 110 °C to remove moisture in the sample pores (Sang et al., 2018a). N_2 adsorption/desorption isotherms of nineteen shales, before and after Soxhlet extraction, were measured at −196 °C using QuadraSorb Station 4 Instrument

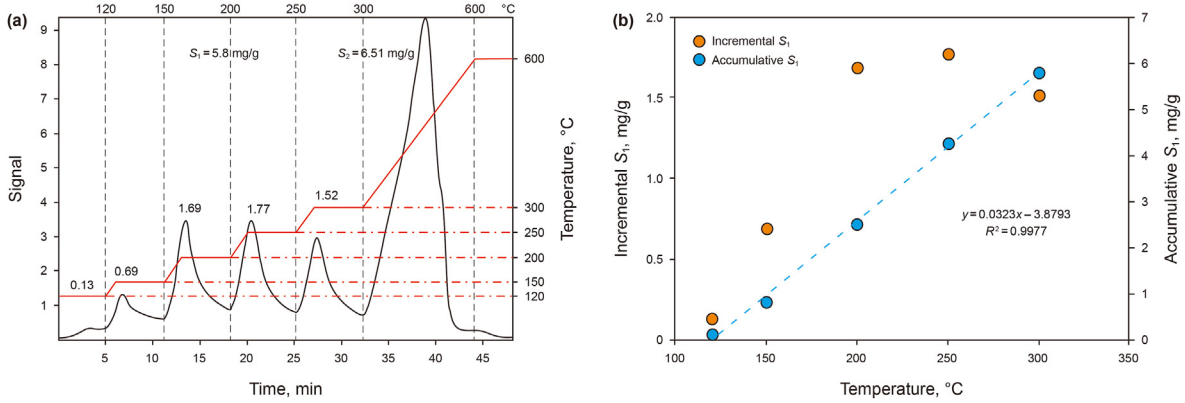

Fig. 7. The multi-step pyrolysis allows the separation of five peaks for the original S_1 peak on the thermogram. The five peaks represent each temperature fraction (120, 150, 200, 250, and 300 °C).

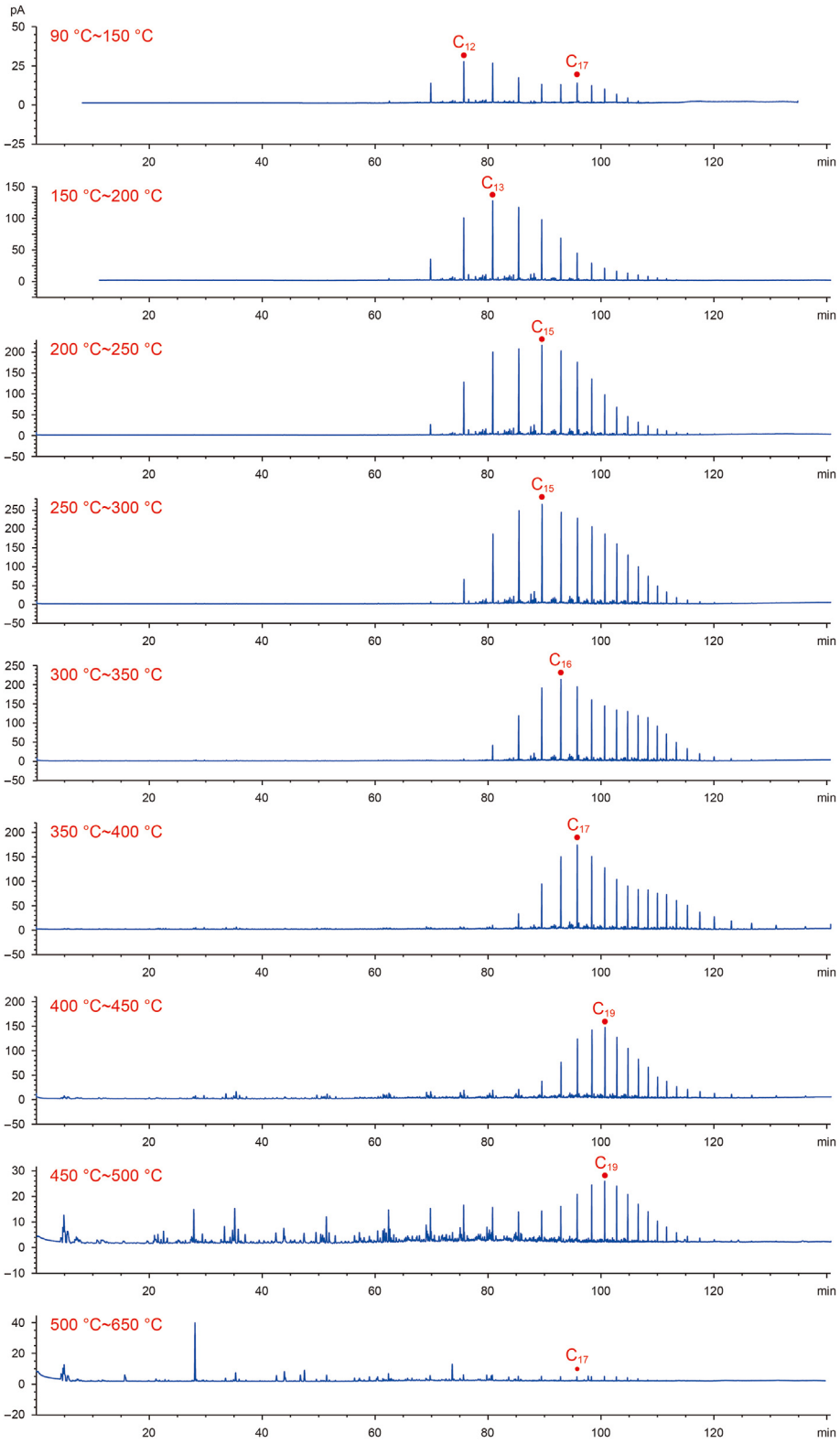

Fig. 8. Pyrolysis gas chromatography depicts the hydrocarbon constituents vaporized at different temperature phases. The basic information of the sample are as follows: TOC = 3.09%, S_1 = 5.02 mg/g, S_2 = 7.57 mg/g, T_{max} = 453 °C, R_o = 1.41%.

in Beijing Center for Physical & Chemical Analysis. The specific experimental procedure is described by Zhang et al. (2020a).

3.7. Pyrolysis gas chromatography (Py-GC)

Py-GC analysis of shale samples was performed on a CDS-6150 Pyroprobe (USA) connected to an Agilent 7890 A GC inlet by a transfer line at 300 °C. Shale sample powders (about 40 mg)

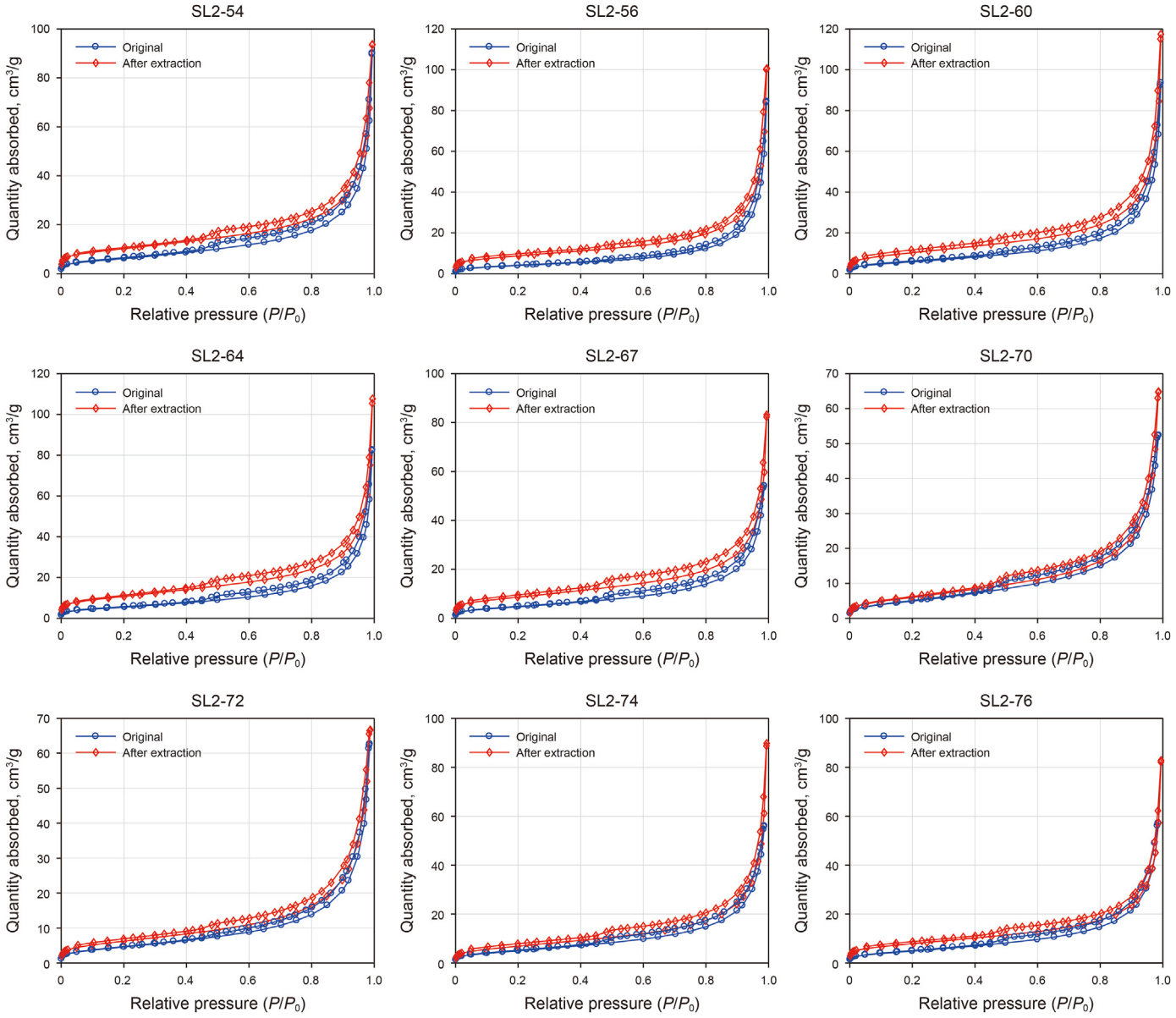

Fig. 9. Typical low-temperature N_2 adsorption/desorption isotherm curves of shales before and after solvent extraction in the Qingshankou Formation, Gulong Sag.

without extraction were loaded into a quartz tube and then placed into the pyrolysis apparatus. The pyroprobe was heated from the initial 90 °C–150 °C at 25 °C/min and held for 10 min to make the hydrocarbons released ultimately. Then it was heated from 150 to 200 °C, 200–250 °C, and sequentially heated until 500–650 °C (heating rate = 25 °C/min), each held for 10 min respectively. A PONA capillary column (50 m × 0.2 mm × 0.5 μm) was used to separate hydrocarbons for gas chromatography. The front part was placed into a liquid nitrogen cold trap before and during each pyrolysis process to prevent the generated hydrocarbon from flowing into the column. The GC oven temperature was initially at 35 °C (held for 10 min) and ramped to 70 °C at the rate of 1.5 °C/min, then raised to 180 °C at the rate of 3 °C/min, and finally increased to 310 °C at the rate of 5 °C/min and held isothermally for 10 min. Hydrocarbons were detected using an FID equipped with a H_2 combustion gas. Both the GC inlet and FID temperatures were set at 300 °C.

4. Results

4.1. Shale oil occurrence and geochemical components

4.1.1. Microscopic oil characteristics

The oil distributes heterogeneously in the pore spaces of shales. Abundant oil was found in the argillaceous matrix compared with the minimal occurrence in the strongly cemented sandy lens or laminae (Fig. 3a). Microscopically, the observation on the occurrence of crude oil and residual bitumen illustrates that most of the shale oil tends to show up in the pores of the clay mineral matrix, which mainly includes the intergranular pores of clay aggregates and intercrystalline pores of clay minerals (Fig. 3b–f). We also found that shale oil exists in the intergranular pores between the weakly cemented terrigenous clastic grains and in the dissolution pores at the edges or inner part of feldspar and plagioclase particles (Fig. 3g–i). Additionally, small amounts of precipitated oil exist in the intercrystalline pores of pyrites (Fig. 3j) and intragranular pores of ostracod shells (Fig. 3k–l). Micro-

Table 1
Pore structure parameters of the Qingshankou un-extracted and extracted shales obtained by LPNA.

Sample ID	Before extraction				After extraction			
	Weight, g	BET surface area, m^2/g	Total pore volume at $P/P_0 = 0.99$, cc/g	Average pore diameter, nm	Weight. g	BET surface area, m^2/g	Total pore volume at $P/P_0 = 0.99$, cc/g	Average pore diameter, nm
SL2-52	1.145	22.06	0.1411	25.58	1.089	36.54	0.1540	16.86
SL2-54	1.031	22.25	0.1397	25.11	1.896	36.03	0.1453	16.13
SL2-55	0.982	22.58	0.1134	20.10	2.505	32.64	0.1591	19.49
SL2-56	0.655	15.15	0.1310	34.58	0.809	31.13	0.1560	20.04
SL2-58	0.526	19.32	0.1343	27.82	1.045	35.02	0.1718	19.63
SL2-59	0.447	23.97	0.1528	25.50	1.048	27.78	0.1765	25.41
SL2-60	0.339	22.05	0.1450	26.30	0.146	36.81	0.1821	19.79
SL2-64	0.851	19.03	0.1281	26.93	0.170	38.44	0.1669	17.37
SL2-66	0.857	12.37	0.0746	24.13	0.344	27.64	0.1835	15.44
SL2-67	0.944	17.99	0.0837	18.62	0.401	31.11	0.1290	16.58
SL2-69	0.558	21.43	0.1359	25.36	0.415	30.17	0.1545	20.48
SL2-70	0.449	19.62	0.0812	16.56	0.444	23.04	0.1006	17.46
SL2-72	0.339	17.34	0.0969	22.35	0.401	22.97	0.1031	17.96
SL2-74	0.316	19.39	0.0868	17.90	0.367	25.57	0.1392	17.66
SL2-75	0.364	19.30	0.0892	18.48	0.450	25.43	0.1322	20.80
SL2-76	0.414	19.14	0.0887	18.53	0.654	28.25	0.1284	18.17
SL2-79	0.376	20.51	0.0921	17.97	0.472	32.41	0.1443	17.81
SL2-81	0.337	19.42	0.0882	18.16	0.539	24.26	0.0981	16.17
SL2-84	0.389	14.47	0.0753	20.81	0.620	15.15	0.0769	20.30

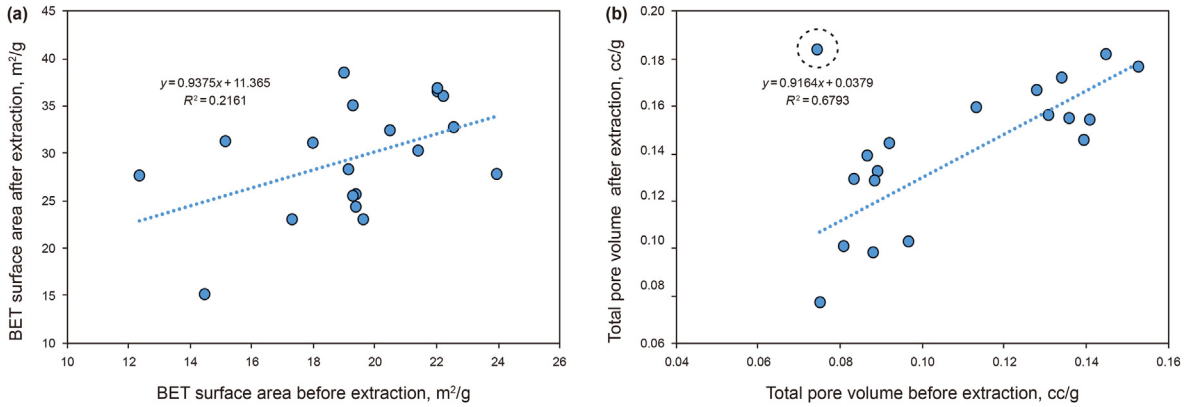

Fig. 10. Correlation between the pore structure parameters of shale samples before and after extraction.

fractures are one of shale oil's most significant storage spaces and migration pathways. The SEM observation shows that parts of the micro-fractures are filled with oil (Fig. 3m–n), and oil films are attached to the edges of micro-fractures (Fig. 3o).

Oil fails to exist in the entire pore system of the shale matrix due to its large molecular size. Thus, understanding the dominant pore spaces for the occurrence of shale oil is crucial to its productivity (Xu et al., 2022). MAPS technology was applied to acquire high-resolution and large formatted SEM images to capture OM occurrence and quantitatively investigate the pore spaces bearing shale oil. Firstly, the area of interest of the sample was divided into multiple tiles, and backscattered electron (BSE) images were recorded sequentially. Then, minerals, pores, and organic matter (including solid OM and residual oil) were segmented by different grayscale cutoff values. They were 0–32 for pores, 33–85 for OM, and 86–255 for minerals in this study. Finally, the volume of each material was calculated statistically based on the images.

To mitigate the influence of similar field depth and grayscale on quantification, particularly the neighboring grayscale values between the residual oil/bitumen and solid organic matter, the BSE images of a shale sample were divided manually into three types based on the occurrence of organic matter. Type I (124 images) contains large chunks of solid OM (Fig. 4a and b). Type II (163 images) represents shales whose pores were filled with macromolecular heavy oil (Fig. 4c and d). Type III (554 images) refers to the shales with no residual oil or solid OM (Fig. 4e and f). The areas with minerals, OM, and pore spaces were segmented and counted. Overall, the percentages of minerals, pore spaces, and organic matter are 97.38%, 0.60%, and 2.02%, respectively.

To investigate the oil film thickness in the pore spaces, the diameters of pores before and after filling with oil were measured and compared based on Type II images. The average diameter of the original shale reservoir pore spaces is 65 nm. In contrast, the pore diameter decreases to 50 nm after the generation and filling of oil in the pores (Fig. 5). The reduction of the average pore size can be considered as the pore spaces occupied by residual oil, indicating that the thickness of the existing oil film is averagely 7.5 nm.

4.1.2. Geochemical characteristics of shale oil components

The oil in the Qingshankou shales, Gulong Sag, shows the characteristics of light hydrocarbon with a high gas-to-oil ratio. The maximum value of the ratio is over 500 m^3/m^3. The density of the

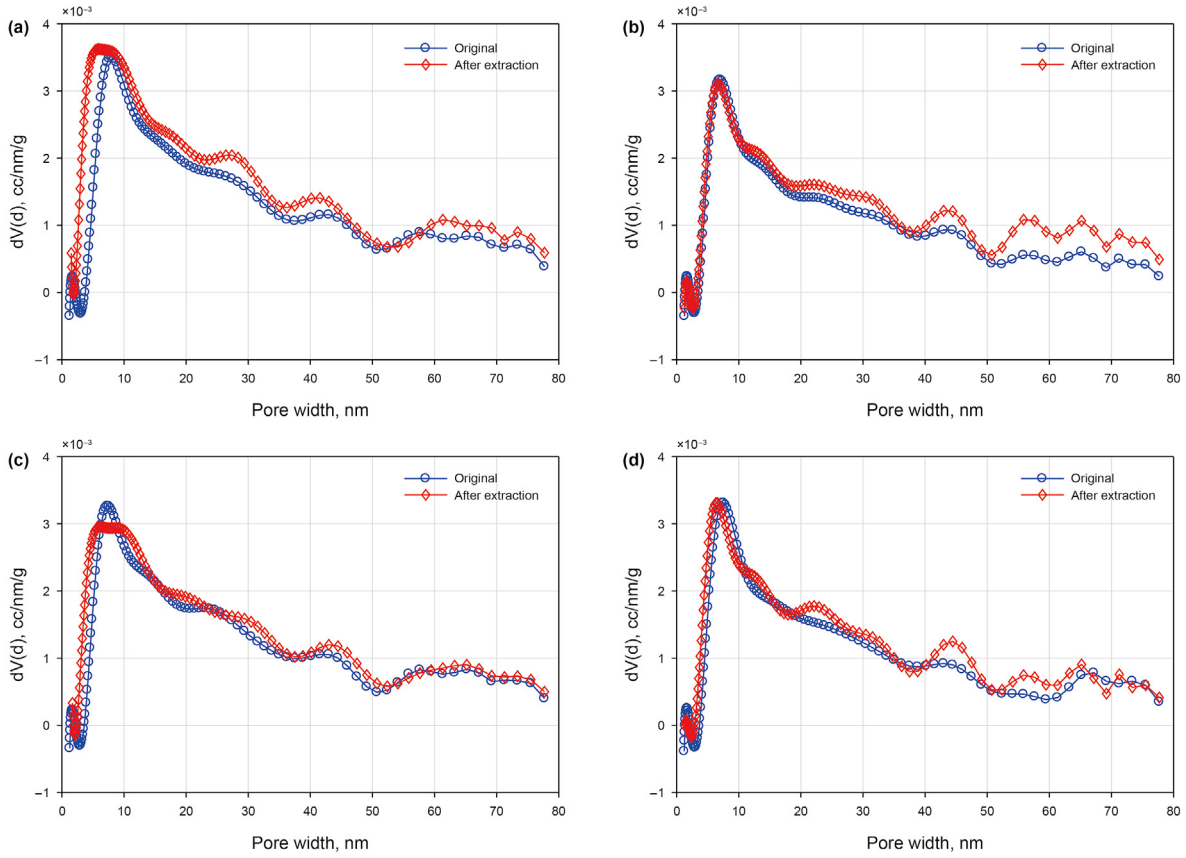

Fig. 11. Pore size distribution variations of the shale samples before and after solvent extraction. (a) Clay mineral-laminated shales, SL2-60; (b) Felsic-laminated shales, SL2-70; (c) Ostracod-laminated shales, SL2-69; (d) Mixed-laminated shales, SL2-81.

Table 2
Signal intensity and quantitative analysis results of the 2D-NMR map in the Qingshankou shale.

Sample ID	Depth, m	Weight, g	Signal intensity, a.u.			Absolute quantity, mg/g rock		
			Region 1	Region 2	Region 3	Region 1	Region 2	Region 3
SL2-54	2343.0	15.14	759.75	111.61	3287.65	20.02	2.36	86.63
SL2-56	2345.5	12.63	783.88	361.86	2292.83	20.66	7.67	60.42
SL2-60	2350.0	12.15	595.04	136.04	2789.78	15.68	2.88	73.51
SL2-64	2353.0	13.21	1147.62	221.94	2904.59	30.24	4.70	76.54
SL2-66	2354.0	16.18	734.84	455.02	2236.60	19.36	9.64	58.94
SL2-67	2355.0	12.76	949.81	234.55	2653.83	25.03	4.97	69.93
SL2-70	2358.0	16.29	491.27	156.18	2306.60	12.95	3.31	60.78
SL2-72	2359.4	10.06	756.83	309.01	2303.19	19.94	6.55	60.69
SL2-74	2361.4	17.73	673.12	211.66	2769.01	17.74	4.48	72.96
SL2-76	2363.4	11.72	602.08	211.99	2302.14	15.86	4.49	60.66
SL2-81	2367.6	16.15	708.78	126.45	2448.71	18.68	2.68	64.52

crude oil ranges from 0.77 to 0.81 g/cm^3, with an average value of 0.79 g/cm^3, and its kinematic viscosity at 50 °C ranges from 1.53 to 4.08 mm^2/s, with an average value of 2.44 mm^2/s. Accordingly, the Qingshankou shale oil is categorized as light crude oil. The crude oil is high in paraffin content, which varies from 7.6% to 22.7% and averages 13%. It consists primarily of saturated hydrocarbon (>90%). The relative percentage of the saturated, aromatic, and NSO components indicates that the Qingshankou shale oil is classified into paraffinic oils (Tissot and Welte, 1984) (Fig. 6).

Multi-step pyrolysis in conjunction with Py-GC is a valuable tool for quantitatively investigating the content and components of hydrocarbons volatilized at gradually increasing temperatures. The analysis shows that the amount of thermally desorbed hydrocarbon at T < 150 °C was relatively low (Fig. 7), indicating the loss of large amounts of evaporative gaseous and light hydrocarbons. Consistently, we observed a lack of hydrocarbons with low carbon number (<C_{10}) in the gas chromatogram (Fig. 8). The original S_1 peak was separated into five peaks, each representing the fraction at the temperature of 120, 150, 200, 250, and 300 °C set by heating program (Fig. 7a). The incremental S_1 exhibited a trend of increase at first and then decreased as the temperature went up. The maximum amount of volatile free hydrocarbon was observed at 200–250 °C. The accumulative S_1 values positively correlate with the temperature with a correlation coefficient of 0.9977 (Fig. 7b).

The component of vaporized hydrocarbon depends heavily on the applied pyrolysis temperature, where higher temperature favors the generation of longer-chain hydrocarbon (Fig. 8). Hydrocarbons were primarily in the physical, thermal desorption process at the temperature below 350 °C, and the dominant components of the free hydrocarbon were in the range of C_{11} ~ C_{28}. When the

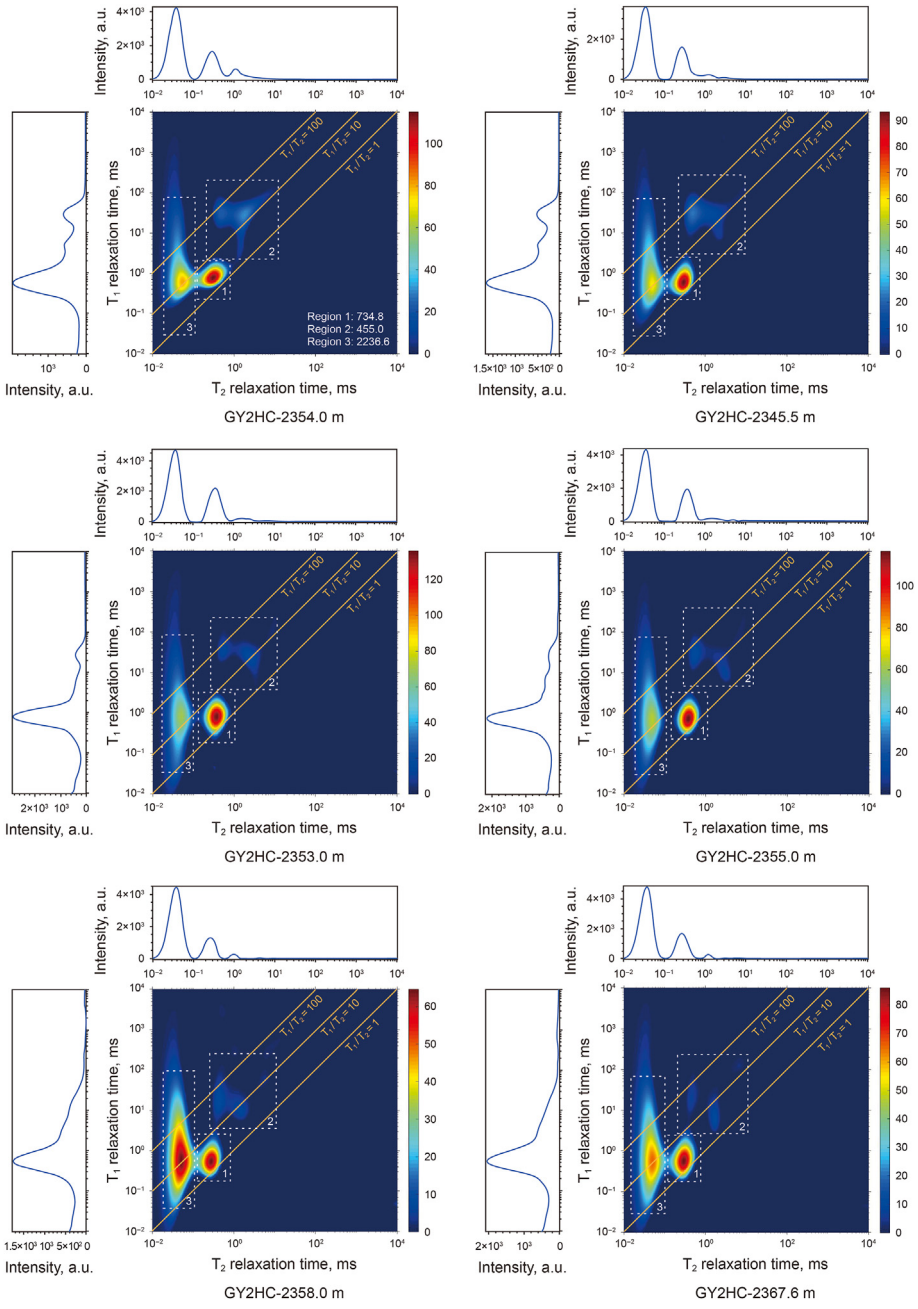

Fig. 12. NMR 2-D maps of oil-bearing shales in the Qingshankou Formation.

applied temperature was higher than 350 °C, the long-chain saturates started to crack, and some hydrocarbons with small molecules or short-chains appeared. Following the increasing temperature, the degree of hydrocarbon thermal decomposition gradually increased. The heavy hydrocarbon was completely cracked when the shale reached an extremely high maturation (T = 650 °C) (Fig. 8).

4.2. Effective pore spaces for shale oil occurrence

4.2.1. Pore structures of the Qingshankou shales

The gas adsorption isotherms of the selected Qingshankou shale samples before and after solvent extraction are illustrated in Fig. 9 as the functions between the quantity of adsorbed N_2 and P/P_0. The isotherm shape of each sample before and after extraction exhibits similar characteristics. However, the quantities of adsorbed gas are different. For each sample under the same relative pressure condition, shales after extraction have more adsorbed gas with varying degrees than the corresponding original samples (Fig. 9).

The gas adsorption-desorption isotherm curves exhibit a hysteresis loop at the relative pressures between 0.4 and 0.5, indicating the multilayer range associated with capillary condensation in mesopores (Schmitt et al., 2013; Tang et al., 2016). Considering the patterns of the hysteresis loops, we suggest that the Qingshankou shales are type H3, which is associated with the slit-shaped pores in the aggregates of plate-like particles (Janssen et al., 2011; Kuila and Prasad, 2013; Schmitt et al., 2013; Sing, 1985).

We compare the specific surface area (SSA), total pore volume,

Table 3
Bulk organic geochemical data for shales in the Qingshankou Formation, Gulong Sag.

Sample ID	Depth, m	Bitumen "A", w.t.%	Unextracted rocks					Extracted rocks				
			TOC, %	S_1, mg/g	S_2, mg/g	T_{max}, °C	S_1+S_2, mg/g	TOC*, %	S_1*, mg/g	S_2*, mg/g	T_{max}*, °C	S_1*+S_2*, mg/g
SL2-54	2343.00	0.77	2.35	3.47	4.01	385	7.48	1.49	0.04	0.30	454	0.34
SL2-56	2345.50	1.25	3.97	5.61	4.72	402	10.33	3.23	0.04	0.58	434	0.62
SL2-60	2349.95	0.71	2.19	2.08	2.87	406	4.95	2.88	0.02	1.17	467	1.19
SL2-64	2353.00	0.69	2.30	3.43	3.62	411	7.05	1.59	0.02	0.30	446	0.32
SL2-66	2354.00	1.21	4.26	8.10	7.30	305	15.40	3.01	0.04	1.21	464	1.25
SL2-67	2355.00	0.82	2.87	4.26	3.95	411	8.21	2.18	0.04	0.51	451	0.55
SL2-70	2358.00	0.46	1.97	2.72	2.62	390	5.34	1.74	0.02	0.49	450	0.51
SL2-72	2359.42	0.91	3.70	6.21	5.23	310	11.44	2.79	0.03	0.61	451	0.64
SL2-74	2361.42	0.67	3.48	4.65	4.33	338	8.98	2.72	0.03	0.59	451	0.62
SL2-76	2363.42	0.69	2.54	3.54	3.40	417	6.94	2.68	0.02	0.57	452	0.59
SL2-81	2367.60	0.55	1.99	3.19	2.99	378	6.18	1.50	0.02	0.28	451	0.30

Note: * – data of extracted samples.

and average pore parameters of the same shale samples before and after extraction (Table 1). The SSA parameters were calculated from the adsorption isotherms based on the modified BET theory (Brunauer et al., 1938). The BET SSA of the original shales ranges between 12.37 and 23.97 m^2/g, with an average value of 19.34 m^2/g. In comparison, the BET SSA of the extracted shales ranges between 15.15 and 38.44 m^2/g, with an average value of 29.44 m^2/g. The total pore volume of the original shales ranges between 0.0746 and 0.1528 cc/g, with an average value of 0.1094 cc/g. In contrast, the extracted samples are between 0.0769 and 0.1835 cc/g, with an average value of 0.1422 cc/g. Overall, both the BET surface area and total pore volume of the shales increase after extraction (Fig. 10).

4.2.2. Effective pore size distribution for shale oil

Pore-scale oil distribution is studied based on the results from the integrated analysis of the solvent extraction and LPNA. In particular, the effective microscopic pore spaces for accumulating shale oil can be estimated by comparing the pore size distribution of shales before and after solvent extraction. The increment of the total pore volume of the extracted samples shows a positive correlation with the quantity of the chloroform bitumen "A", indicating the pore spaces are filled with shale oil in situ.

The micro-oil in different lithofacies is distributed in pore spaces of various sizes. In clay mineral-laminated shales, the volume of pores smaller than 7 nm increases significantly after dichloromethane extraction. Additionally, the pores between 20 and 45 nm and larger than 60 nm increase after extraction (Fig. 11a). It illustrates that shale oil in the CLS is almost distributed in the pores of full range. In felsic-laminated shales, the volume of pores larger than 50 nm increases significantly, while that of the pores between 20 and 50 nm increases slightly after extraction (Fig. 11b). In ostracod-laminated shales, no prominent increment of pore spaces after solvent extraction is observed. Only a very slight increase in the pore volume is observed for pores of 25–50 nm in size (Fig. 11c). This indicates that a tiny amount of the shale oil is filled in the pores of OLS, which is consistent with the low content of chloroform bitumen "A". In the mixed-laminated shales, the pore volume between 20 and 25 nm and 40–65 nm increases significantly (Fig. 11d). Overall, the CLS contains the largest volume of pores with the greatest variations of pore size associated with shale oil (<10 nm, 20–45 nm, and >60 nm). On the contrary, the OLS has the fewest pores preserving oil with a very minimal variation in pore size. The shale oil tends to distribute more likely in larger pores (>50 nm) in the FLS, while shale oil is stored at various and transitional pore size distribution in the MLS as it comes from a mixture of the other lithofacies.

4.3. NMR 2-D mapping of shales

The NMR 2-D mapping results are displayed in Table 2 and Fig. 12, demonstrating the distribution of ^1H at different phases in the Qingshankou shales. The response signals are divided into three parts based on the characteristics of 2-D NMR (Fig. 12). Region 1 shows a T_1 relaxation time between 0.2 and 2 ms, a T_2 relaxation time between 0.1 and 1 ms, and a T_1/T_2 ratio between 1 and 10. Region 2 shows the characteristics of a $T_1 > 2$ms, a $T_2 > 0.2$ ms, and a T_1/T_2 ratio between 1 and 100 mostly. It is likely to be in the oil position, according to Khatibi et al. (2019), although there is some deviation in location. Region 3 has the shortest T_2 (smaller than 0.1 ms), a wide range of T_1 (0.1–10 ms), and a high T_1/T_2 ratio, interpreted as a hydroxyl-rich compound in previous studies, including a structured kerogen molecule, a macromolecular branch of heavy oil or inorganic OH- (hydroxyl) (Khatibi et al., 2019; Liu et al., 2019).

5. Discussion

5.1. Total residual oil content evaluation

5.1.1. Chloroform bitumen "A" extraction method

Chloroform bitumen "A" (abbreviated as "A") refers to the soluble OM in sedimentary rocks, whose content is represented by the mass ratio of the amount of bitumen extracted by the dichloromethane to the quantities of the extracted rock sample powders (Eq. (1)), expressed as mg/g rock. As a comprehensive result of hydrocarbon generation and expulsion, the content of "A" reflects the total residual oil amount retained within the shale pore spaces, consisting of both movable and adsorbed hydrocarbons. According to the experimental data, the total residual oil content ranges from 4.6 to 12.5 mg/g rock, with an average value of 7.9 mg/g.

$$\sigma_1 = A/m \tag{1}$$

where σ_1 is the amount of the extracted total residual oil, mg/g rock; A is the chloroform bitumen "A" mass, mg; and m indicates the mass of shale samples extracted, g.

5.1.2. Pyrolysis method based on unextracted and post-extracted shales

The standard programmed pyrolysis in the open system has been widely used to assess the amount of hydrocarbon resources or original oil in place, especially for unconventional shale and tight oil resources (Jiang et al., 2016; Wang et al., 2022). In traditional petroleum geology, the pyrolysis S_1 peak represents the free hydrocarbon, which was volatilized during a temperature lower than 300 °C. The S_2 peak represents the hydrocarbon generated by

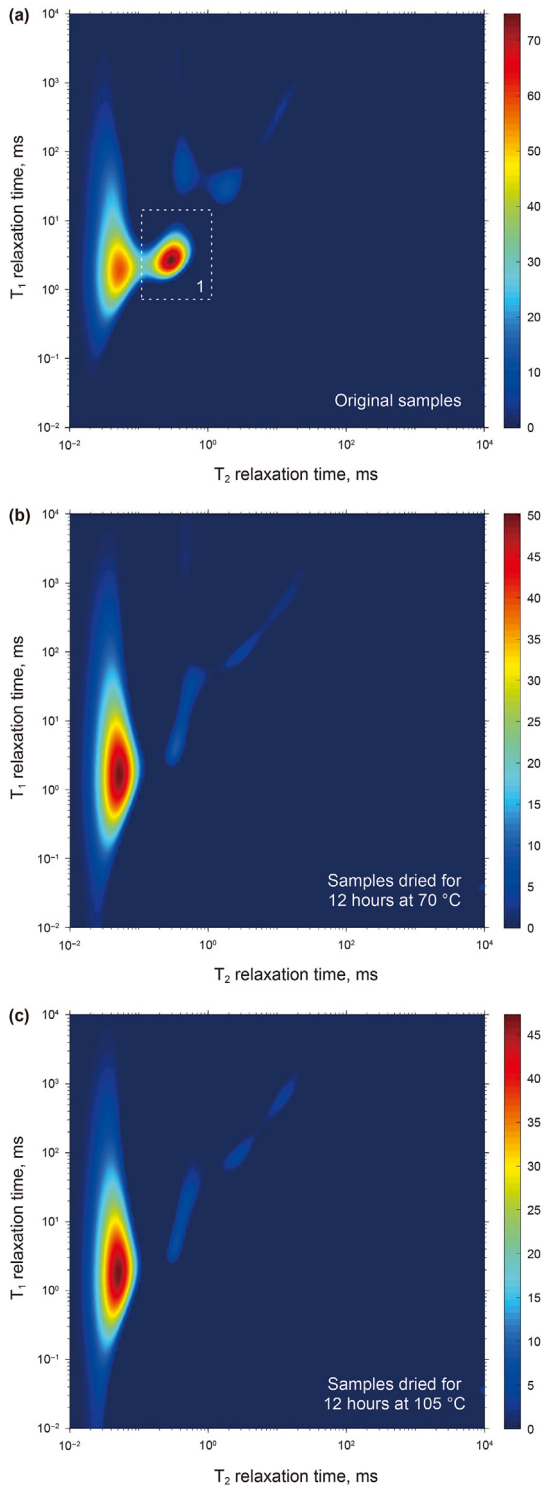

Fig. 13. NMR 2-D maps of shale samples in the original state and dried at different temperatures.

kerogen cracking from 300 to 650 °C (Tissot and Welte, 1984). However, questions still exist, such as whether the thermally desorbed hydrocarbon at a temperature lower than 300 °C could include all of the generated hydrocarbons in the fine-grained sedimentary rocks. Therefore, pyrolysis for unextracted and post-solvent extracted samples was combined to estimate the total residual oil content in the Qingshankou shales.

According to Table 3, the Rock-Eval S_1 values were decreased to 0.03 mg/g, and the S_2 values were reduced by more than 80% after dichloromethane extraction, which illustrates that the total residual oil in high-maturity shales includes all of the S_1 and most of the S_2. Therefore, an evaluation index of the total residual oil content by pyrolysis is applied (Eq. (2)).

$$\sigma_2 = S_1 + S_2 - S_2^* \quad (2)$$

where σ_2 is the pyrolytic total residual oil content, mg/g; S_1 is the free hydrocarbon for unextracted samples, mg/g; S_2 and S_2* are the pyrolyzed hydrocarbon for unextracted and extracted samples, respectively, mg/g. The total residual oil content calculated by the pyrolysis method ranges from 3.8 to 14.2 mg/g, with an average value of 7.8 mg/g, which is very close to the content of the extracted total oil (7.9 mg/g).

5.2. Shale oil occurrence state and mobility evaluation

5.2.1. Fluid component identification

Previous studies have interpreted signal intervals of the different components on the T_1-T_2 maps (Fleury and Romero-Sarmiento, 2016; Khatibi et al., 2019; Liu et al., 2019; Washburn and Birdwell, 2013). However, samples of different maturity, mineral composition, pore structures, or even from different regions behave distinctively in fluid component response, such as their types, signal location, and amplitude. In this study, we used a series of methods to demonstrate precisely the meaning of the response in each region in the Qingshankou shales.

An original sample was conducted on 2-D NMR quantitative analysis to investigate the water component of the shale. Then, the sample was heated at 70 °C for 12 h for the second NMR measurement. Finally, it was heated at 150 °C for 12 h for the third measurement. The signals of Region 1 disappeared after the shale was dried at 70 °C for 12 h (Fig. 13a and b), considered as water in nanopores or micro-cracks.

The signal intensity of Region 3 (Fig. 12), which was interpreted as a hydroxyl-rich compound by previous studies (Khatibi et al., 2019; Liu et al., 2019), changed very slightly following the heating process (Fig. 13b and c). However, the amplitude of Region 3 is positively correlated with total clay mineral content (Fig. 14a), particularly for the content of I (R^2 = 0.63) and I/S (R^2 = 0.31) (Fig. 14b and c). Furthermore, the amplitude is best correlated with the sum of I and I/S (R^2 = 0.74) (Fig. 14d). This indicates that the hydrogen signals of Region 3 are mainly contributed by clay minerals with hydroxyl groups (OH) in their crystallographic lattice structure, or water of crystallization (Fleury et al., 2011; Zhang et al., 2020b), particularly may arise from water molecules trapped in empty potassium sites between the layers of illite or hydroxyl groups in illite crystalline structure, which has a formula of $K(Al_2)(Si_3Al)O_{10}(OH)_2$ (Fleury et al., 2011; Khatibi et al., 2019; Li et al., 2020b).

Region 2 was interpreted as oil zones by previous studies (Khatibi et al., 2019; Li et al., 2020b; Washburn and Birdwell, 2013; Washburn and Cheng, 2017). Our study also demonstrated that the oil content parameters, such as the chloroform bitumen "A", S_1+S_2−S_2* and S_1 are linearly correlated with the amplitude of NMR Region 2 (Fig. 15a and b), thereby establishing the relevance of Region 2 to oil position. However, it is still controversial whether the signal of the Region 2 represents total oil or movable oil content (Khatibi et al., 2019; Li et al., 2020b; Washburn and Birdwell, 2013; Washburn and Cheng, 2017). Khatibi et al. (2019) translated all signals of Region 2 as movable oil using pyrolysis data for correction when studying on the geochemical properties of the Bakken Formation (Khatibi et al., 2019; Silletta et al., 2022). However, other

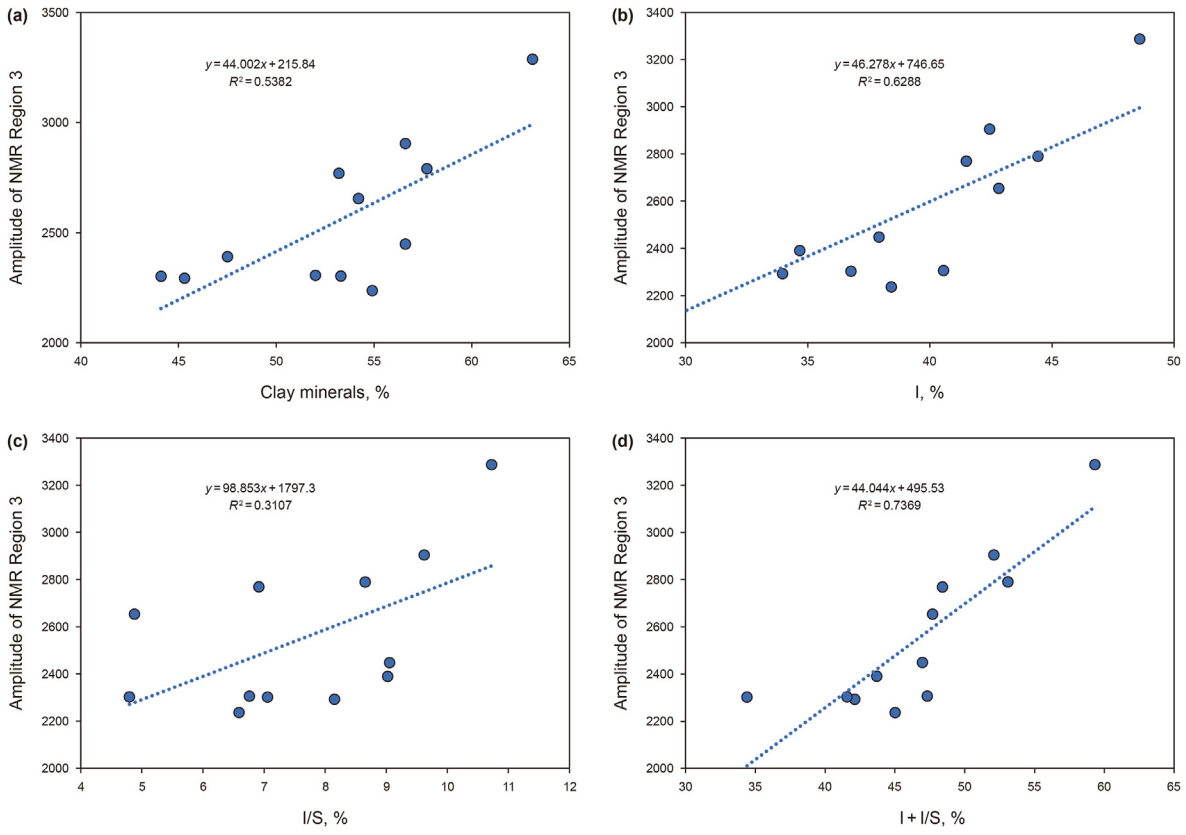

Fig. 14. Relationships between the 2-D NMR amplitude of Region 3 and clay mineral types and content.

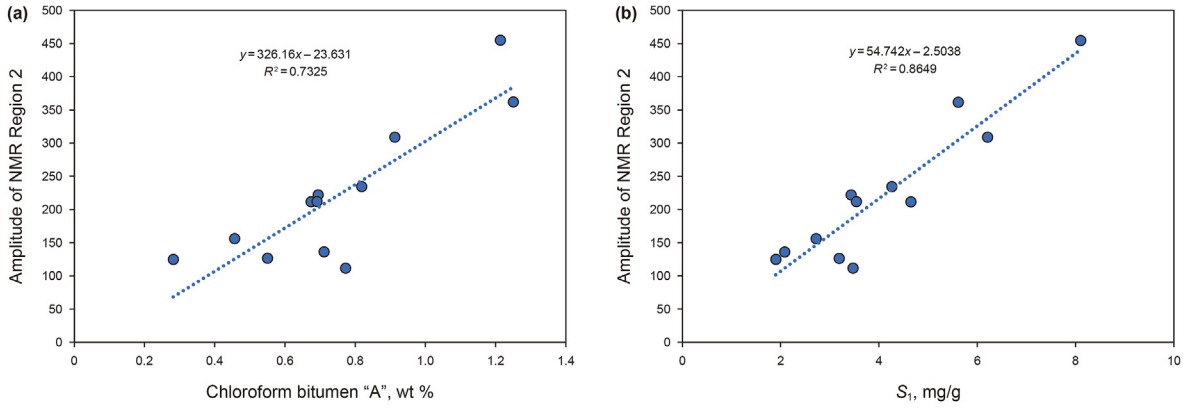

Fig. 15. Plots of the 2-D NMR amplitude of Region 2 and parameters of oil-bearing property.

scholars thought that signals of Region 2 include movable hydrocarbon, which occurs in nano-inorganic micropores with poor connectivity, and adsorbed hydrocarbon in the interior of kerogen (organic pores) or on the surface of hydrophobic kerogen or mineral particles (Li et al., 2018; Li et al., 2020b; Yan et al., 2017). For the highly mature shales similar to the Qingshankou Formation in the Gulong Sag, we prefer to think that signals of Region 2 represent movable oil zones even if the relaxation time of T_1 and T_2 displayed separation (Fig. 12). Crude oil generated by highly mature shales usually shows the characteristics of low density and viscosity, high gas-oil ratio, and high content of light and saturated hydrocarbon (Sun et al., 2021), resulting in highly movable of the shale oil. Additionally, Fig. 15 shows that the signal intensity of Region 2 is better positively correlated with the S_1 values ($R^2 = 0.86$) than chloroform bitumen "A" content or $S_1+S_2-S_2$*. The former is considered as an evaluation parameter of movable hydrocarbon content (Jiang et al., 2016; Romero-Sarmiento, 2019) while the latter represent total residual oil content.

Compared with the low-medium mature lacustrine shales, the highly mature Qingshankou shales in the Gulong Sag exhibited almost no signals in Region 4 (Fig. 16a and b). It is characterized by higher T_1 and lower T_2 values due to its low efficiency of transmitting fluctuating energy to the environment and the strong intramolecular polar coupling, which was interpreted as solid OM (or asphaltene) in the previous studies (Washburn and Birdwell, 2013; Khatibi et al., 2019; Silletta et al., 2022). The lack of Region 4 signals probably result from the massive decomposition of sedimentary organic matter at the very high maturity along with the

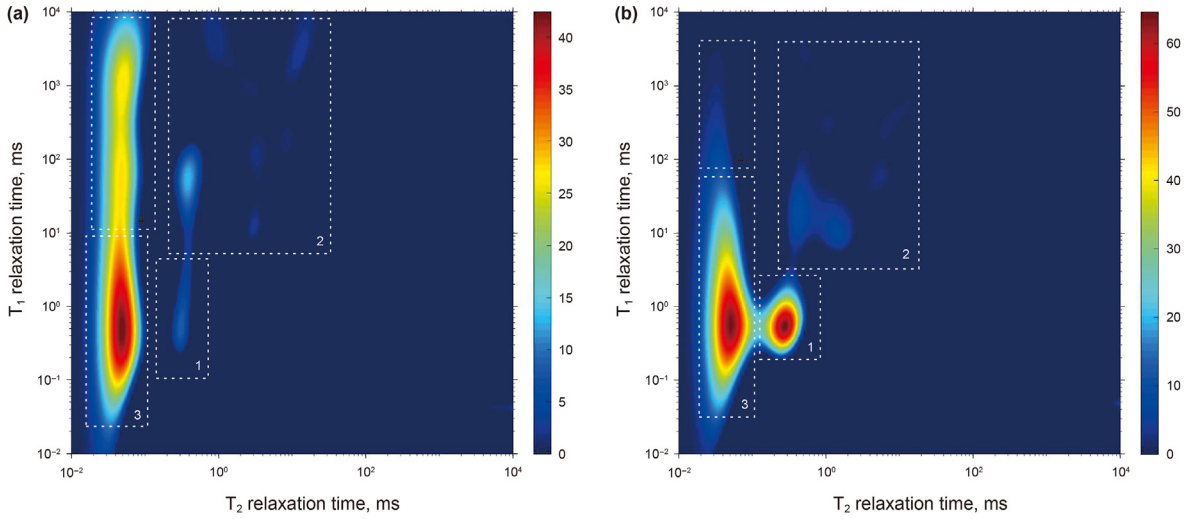

Fig. 16. Comparison of NMR 2-D mappings of shales in low-medium maturity (a) and high maturity (b). (a) the sample from the Chang 7 member in the Ordos Basin, R_o = 0.8%, TOC = 11.47%, clay mineral content = 43.4%; (b) the sample from the Qingshankou Formation in the Songliao Basin, R_o = 1.3%, TOC = 1.97%, clay mineral content = 52%.

Table 4
Shale oil content in different occurrence states in the Qingshankou Formation, Gulong Sag.

Sample ID	Depth, m	Total oil content, mg/g	Movable oil content, mg/g rock	Adsorbed oil content, mg/g rock	Movable oil ratio, %
SL2-54	2343.0	7.7	2.36	5.36	30.6
SL2-56	2345.5	12.5	7.67	4.84	61.3
SL2-60	2350.0	7.1	2.88	4.23	40.5
SL2-64	2353.0	6.9	4.70	2.24	67.7
SL2-66	2354.0	12.1	9.64	2.50	79.4
SL2-67	2355.0	8.2	4.97	3.22	60.7
SL2-70	2358.0	4.6	3.31	1.26	72.5
SL2-72	2359.4	9.1	6.55	2.58	71.7
SL2-74	2361.4	6.7	4.48	2.26	66.5
SL2-76	2363.4	6.9	4.49	2.42	65.0
SL2-81	2367.6	5.5	2.68	2.82	48.7

generation of large amounts of pore water, as shown in Region 1 of Fig. 16b.

5.2.2. Movable oil content calculation

To quantitatively translate the signal intensity of NMR to the amount of movable oil, the crude oil sample obtained from the Qingshankou shale formation and $CuSO_4$ solution were analyzed by the 2-D NMR under the same experimental condition. The signals of movable oil (Region 2) were calibrated by the 2-D NMR spectrum of the crude oil, whereas the signals of water in nanopores or micro-cracks (Region 1) and water of crystallization (Region 3) were calibrated by $CuSO_4$ solution.

The movable oil content measured by the NMR method for 11 shale samples ranges from 2.36 to 9.64 mg/g rock, with an average value of 4.89 mg/g, slightly higher than the S_1 values (average = 4.1 mg/g). Therefore, we consider that the movable oil in the Qingshankou shales consists of the entire S_1 and a small quantity of S_2. The total residual oil content of the corresponding samples is in the range of 4.6–12.5 mg/g, with an average of 8.0 mg/g, and therefore the adsorbed oil content is between 1.26 and 5.36 mg/g (average = 3.07 mg/g). The movable oil ratio ranges from 30.6% to 79.4%, with an average value of 60.4% (Table 4). It is worth noting that the "movable oil" referred to here is not the same as that in engineering, where the term is more reliable in engineering and fracturing technology (Cudjoe et al., 2016; Altawati et al., 2022; Lei et al., 2022). In this paper, movable oil means the hydrocarbon components of lighter or smaller molecules, which is relatively easier to flow out of the pore spaces.

5.3. Controlling factors on states of shale oil occurrence

5.3.1. Effect of organic matter

Oil and gas are retained within kerogen by adsorbing on the internal surfaces of kerogen or by being physically trapped within a rigid kerogen macromolecule framework (Pepper and Corvi, 1995; Zhang et al., 2019). The adsorption/absorption effect is jointly controlled by the content, type, thermal maturity of OM, and the type of adsorbed organic compounds (Zhang et al., 2012). Following the thermal evolution of OM, the state of the Qingshankou shale oil mainly changes from the adsorbed oil-dominated into free oil-dominated (Zeng et al., 2022). The total shale oil content displays a good positive linear correlation with organic matter abundance (R^2 = 0.75) (Fig. 17a), and the same trend applies to the movable oil content (R^2 = 0.82) (Fig. 17b). The figure illustrates that the indigenous shale oil yield is highly dependent on TOC. The adsorbed oil content also exhibits a positive correlation with TOC, indicating the strong adsorption capacity of the organic matter of the crude oil. However, as the TOC values increase, the ratio of adsorbed oil to total oil in the Qingshankou shales decreases, and the ratio of the movable oil to total oil rises (Fig. 17c), which is contradictory to the results in previous studies (Wang et al., 2019). Wang et al. (2019) has found that the adsorbed oil content increases as the TOC grows up, resulting in decreased proportion of movable oil in the Shahejie Formation in Jiyang Depression (Wang et al., 2019). The

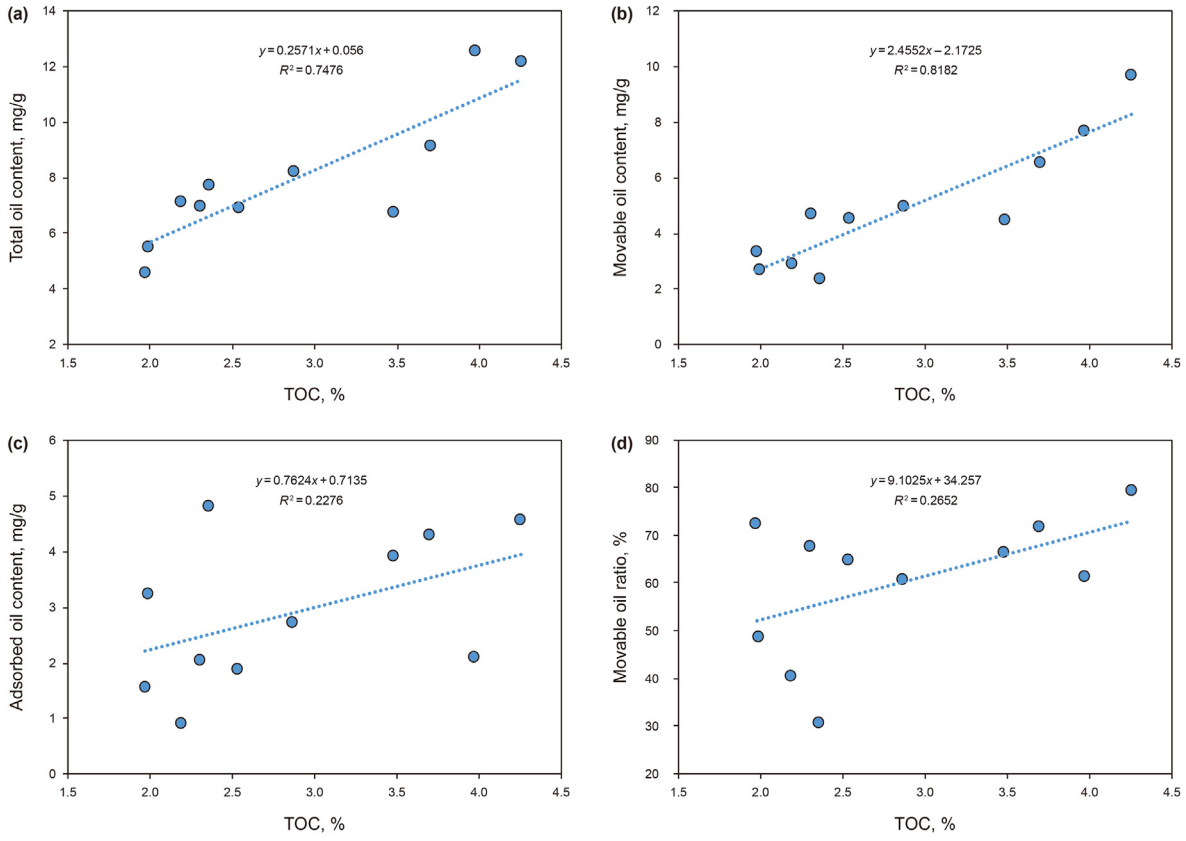

Fig. 17. Relationships between organic matter abundance (TOC) and total shale oil content (a), movable oil content (b), adsorbed oil content (c), and movable oil ratio (d) in the Qingshankou shale.

conflict is probably owing to the maturity of shale oil. Some aliphatic chains, carboxyl groups, hydroxyl groups, and carbonyl groups in crude oil gradually break down following the thermal evolution, resulting in weaker polarity of the highly matured shale oil. Therefore, the oil produced in the highly mature shales has a lower density, viscosity, and more saturated hydrocarbon content than in the low-medium mature shales (Sun et al., 2021). As a result, the interaction force between organic matter and shale oil molecules decreases, leading to weakened oil adsorption capacity onto kerogen's internal surface area, thus lowering the proportion of adsorbed hydrocarbons (Pepper and Corvi, 1995).

5.3.2. *Effect of mineral composition*

The Qingshankou shales in Gulong Sag contain very high content of clay minerals (exceeding 50%), which is different from Barnett Shales and Bakken Shales in the U.S., as well as Paleogene Kong-2 Member and Shahejie shales in Bohai Bay Basin, and Permian Lucaogou shales in Junggar Basin in China (Han et al., 2015; Liu et al., 2021b; Zhao et al., 2022). As the dominant mineral components of the Qingshankou shales, clay minerals have unique interlayer structures and a large reactive surface capable of adsorbing significant amounts of organic compounds (Kennedy et al., 2002), which play a critical role in hydrocarbon retention. This is also illustrated by our result of the positive correlation between clay mineral content and adsorbed oil, shown in Fig. 18a. However, the strong adsorption capacity of clay minerals would result in low mobility of shale oil. As a result, the movable oil content has a negative correlation with the amount of clay minerals (Fig. 18b). Meanwhile, the movable oil ratio shows a decreased trend with the increase of clay minerals, especially with the I/S (Fig. 18c). This is due to montmorillonite minerals generally exhibit oil-wetting properties and absorb large amounts of polar components (Barclay and Worden, 2000; Robin et al., 1995).

Felsic minerals in shales are vital to developing shale oil as their brittleness favors artificial fracturing and facilitates shale oil production (Soeder, 2018; Zhang et al., 2019). However, the negative correlation between the amounts of felsic minerals and total oil demonstrates that felsic minerals are unfavorable to shale oil occurrence and storage (Fig. 18d). The intergranular dissolution pores between felsic particles are less developed due to strong calcite or clay mineral cementation in highly mature shale. Furthermore, quartz is preferentially water-wet under normal oil reservoir conditions (pH ranges 4–7) because negatively charged hydroxyl groups project from the surface of the quartz (polar compounds typically have a negative charge) (Barclay and Worden, 2000). Therefore, it has lower adsorption capacity of crude oil, demonstrated by the negative correlation between felsic minerals and adsorbed oil content (Fig. 18e). Although the potassium feldspar (K-feldspar) content is relatively low in the Qingshankou shales, it shows a good negative correlation with the total oil ($R^2 = 0.53$), movable oil content ($R^2 = 0.62$), and the movable oil percentage (Fig. 18f and g). This is probably because intragranular dissolution pores in K-feldspar can offer storage spaces for shale oil, especially for movable oil. The carbonate minerals in the Qingshankou shales mainly consist of calcite, except for only one sample (SL2-56) dominated by ankerite. The amount of carbonate is positively correlated with the total, movable, and adsorbed oil content, probably due to their oil-wet properties (Fig. 18h and i), which is a major factor controlling oil content, distribution, and occurrence states in a reservoir (Anderson, 1986; Barclay and Worden, 2000).

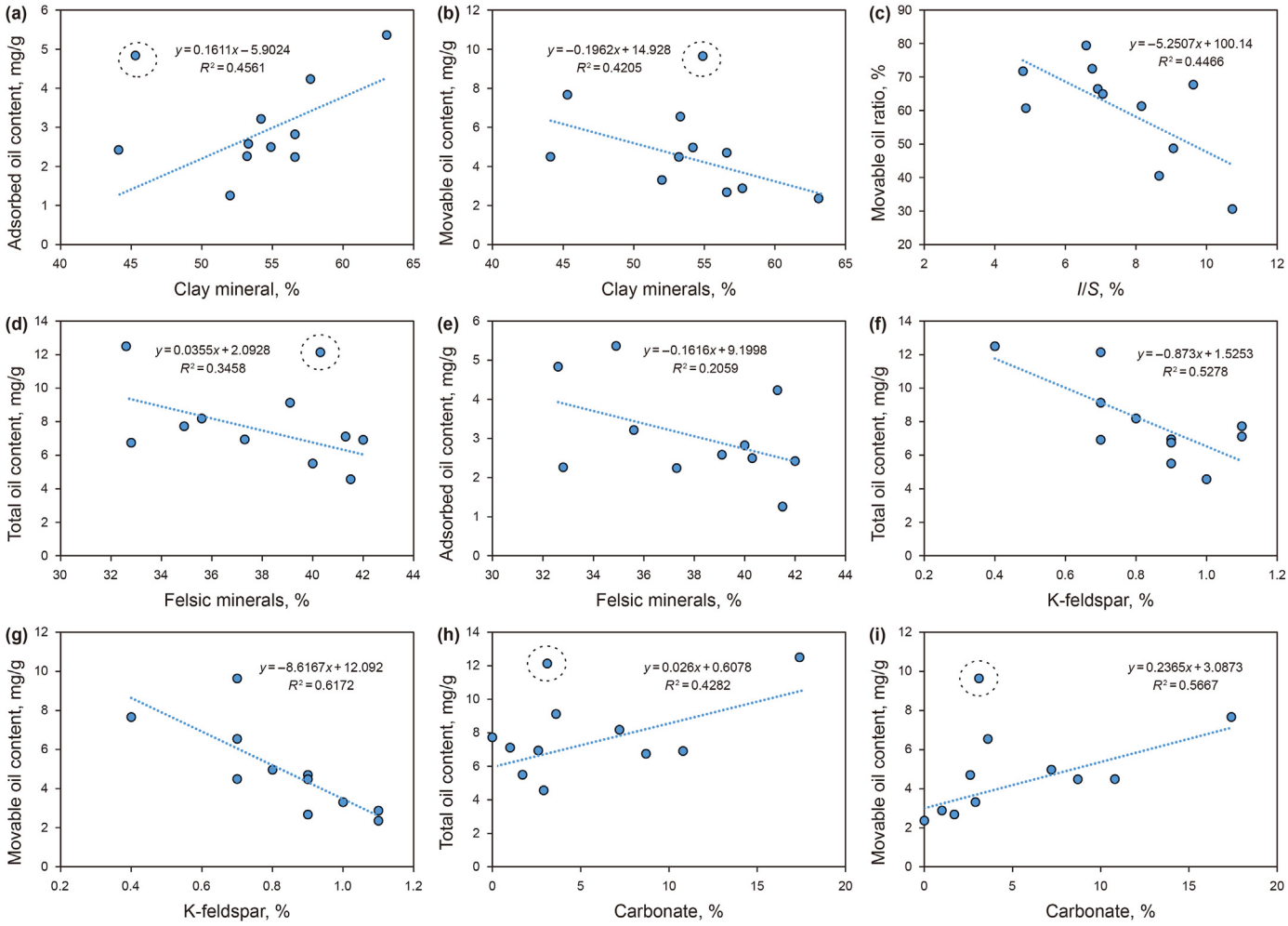

Fig. 18. Relationships between mineral compositions (clay minerals, felsic minerals, and carbonates) and total shale oil content, movable oil content, and movable oil ratio in the Qingshankou shales.

5.3.3. Effect of pore structures

Shales have a complex pore structure because of the multiscale fabric resulting from clay minerals' microstructure. We have clarified the dominant pore-size distribution of the effective pore spaces to preserve the oil as previous description. Except for the pore-size distribution, the pore structure parameters of the shale matrix, such as the specific surface area, average pore diameter, and total pore volume, also affect the shale oil's content and mobility.

The specific surface in shales is the principal place for oil to be preserved (Zhu et al., 2013). Previous studies show that 85% of organic matter is closely related to the specific surface area in black shales (Kennedy et al., 2002; Mayer, 1994). However, the BET SSA demonstrates a linearly negative correlation with the total and movable shale oil content (Fig. 19a and b). It does not mean that shale oil concentration decreases with increased SSA. Instead, oil molecules' physisorption on the external surface of minerals and chemisorption on the inner surface of clay mineral interlayers decrease SSA, which is demonstrated by a significant increment of SSA after solvent extraction (Table 1). The adsorbed oil content associates positively with SSA after extraction (Fig. 19c), illustrating that the shale oil in an adsorption state exists predominately on the surface of clay minerals, organic matter, and pores. Therefore, as the SSA of pores increases, the movable oil ratio descends correspondingly (Fig. 19d).

Fig. 19e–g shows that the average pore diameter positively correlates with the amount of total, movable, and adsorbed oil, indicating that the larger pores are favorable spaces for shale oil accumulation regardless of the oil states. However, no obvious pattern is observed between the ratio of movable oil to total oil with the average pore diameter. The total pore volume also has a weak positive relationship with the total oil content (Fig. 19h). However, it is not correlated with the movable and adsorbed oil content. The total pore volume of shales is negatively correlated with the ratio of movable oil to total oil (Fig. 19i). The larger total pore volume of shales is usually contributed by a greater abundance of micro- or meso-pores. These pores are characterized by larger specific surface area and more robust stronger adsorption capacity, leading to a lower ratio of movable oil.

6. Conclusions

An integrated analysis was conducted on the Qingshankou shales to depict the microscopic occurrence characteristics, the effective pore spaces and pore size distribution of the shale oil, to determine the amount of shale oil in different states, and to define the primary controlling factors (TOC, mineral composition, and pore structure) on the amount and mobility of shale oil. This study improves the understanding of enrichment mechanisms of the highly mature lacustrine shales in pure shale formations, and provides a reference for optimizing favorable shale oil exploration

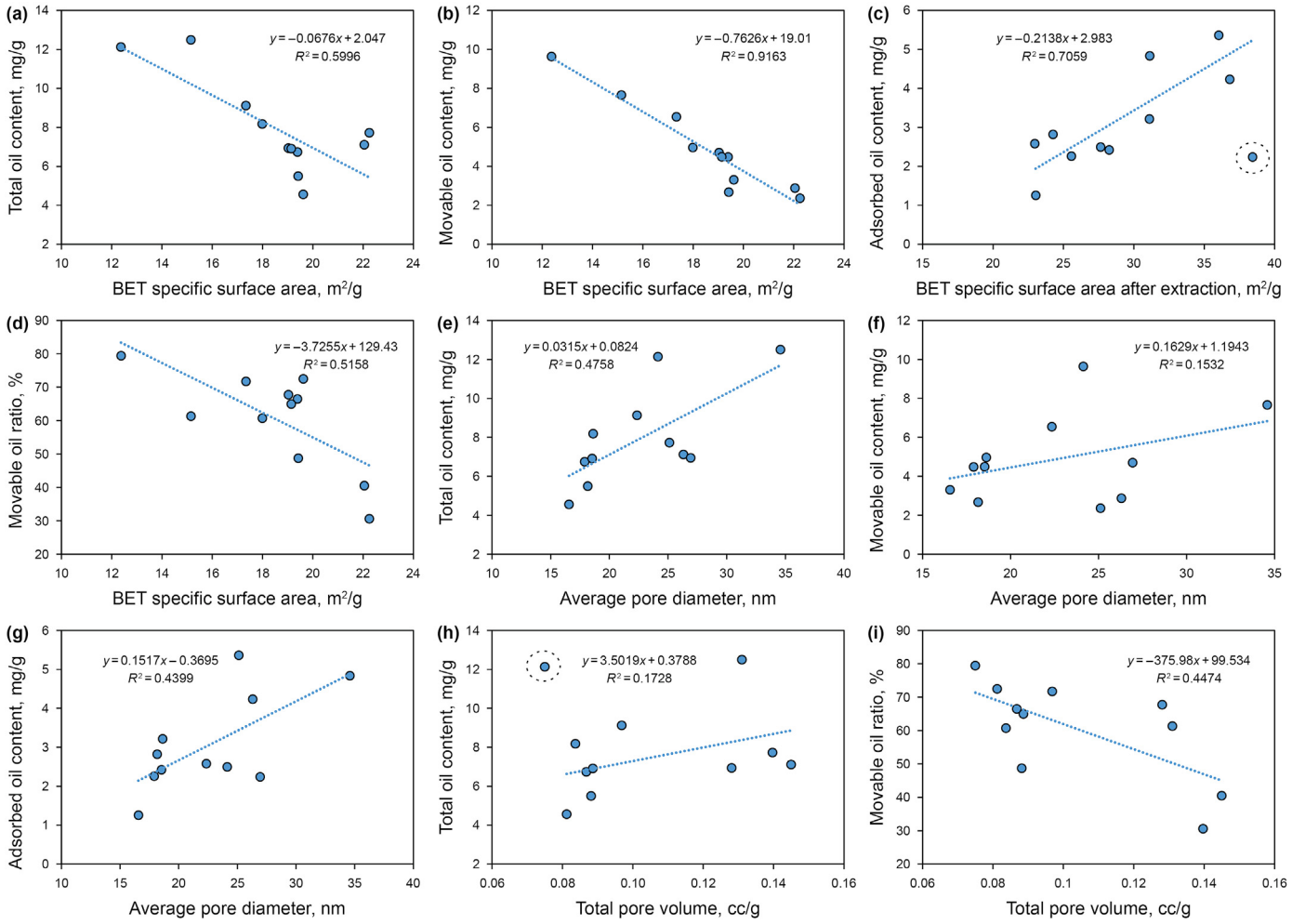

Fig. 19. Relationships between shale pore structures (BET specific surface area, average pore diameter, and total pore volume) and shale oil content in different occurrence states (total, movable, and adsorbed oil) in the Qingshankou shales.

target.

The shale oil distributes heterogeneously in the pore space of shales, mainly in the intergranular pores of clay aggregates and intercrystalline pores of clay minerals, where the unilateral thickness of the existing oil film averages at 7.5 nm. The lithofacies of the Qingshankou shales are divided into four types (CLS, FLS, OLS, and MLS), and the micro-oil in the various lithofacies is distributed in the pore spaces with different sizes. The CLS contains the broadest range and most significant volume of pore spaces with shale oil, whereas the OLS has the narrowest range and fewest pore spaces that preserve shale oil. The FLS tends to preserve shale oil in larger pores (>50 nm), and the oil-bearing pore spaces in the MLS are in the mixture of other lithofacies.

Dichloromethane extraction, Rock-eval pyrolysis, and 2-D NMR are combined to determine the movable, adsorbed, and total residual shale oil contents. The ratio of movable oil to total oil ranges from 30.6% to 79.4%. Multiple controlling factors on the amount of shale oil presenting at different states include TOC, mineral composition, and pore structures of shales. Indigenous shale oil yield and the amount of oil at various states highly depend on OM abundance. Varying types of minerals have noticeable different impact on the states and amount of shale oil. Clay minerals with stronger adsorption capacity result in a higher oil content but lower mobility of shale oil. Felsic minerals have a negative effect on shale oil content in various states. In addition, carbonate plays a significant role in hydrocarbon retention. The amount of carbonate minerals is positively correlated with the total, movable, and adsorbed oil contents, probably due to their oil-wet properties. Pore structures have an essential effect on the amount and state of shale oil. The BET SSA after extraction associates positively with adsorbed oil content, illustrating that the shale oil in the adsorption state exists predominately on the surface of clay minerals and pores. The average pore diameter positively correlates with the total, movable, and adsorbed oil amounts, indicating that the larger pores are favorable spaces for shale oil accumulation. The total pore volume also has a weak positive relationship with the total oil content.

Declaration of competing interest

The authors declare that they have no known competing financial interests or personal relationships that could have appeared to influence the work reported in this paper.

Acknowledgments

This study was funded by the National Natural Science Foundation of China (Project 42090025 and 42202152) and Heilongjiang Province open competition projects: “Research on the shale oil phase state, seepage mechanism, and integrated geological-

engineering stimulation technology in the Gulong Sag" and "Research on the diagenetic dynamic evolution process and its coupling relationship with pores and fractures". We thank Daqing Oilfield Academician Workstation and National Key Laboratory of Continental Shale Oil (NKL-CSO) for providing the cored rock samples and primary data.

References

Abrams, M.A., Gong, C., Garnier, C., Sephton, M.A., 2017. A new thermal extraction protocol to evaluate liquid rich unconventional oil in place and in-situ fluid chemistry. Mar. Petrol. Geol. 88, 659–675. https://doi.org/10.1016/j.marpetgeo.2017.09.014.

Altawati, F., Emadi, H., Khalil, R., Heinze, L., Menouar, H., 2022. An experimental investigation of improving Wolfcamp Shale-Oil recovery using Liquid-N_2-assisted N_2 and/or CO_2 Huff-n-Puff injection technique. Fuel 324, 124450. https://doi.org/10.1016/j.fuel.2022.124450.

Anderson, W.G., 1986. Wettability literature survey - Part 1: rock/oil/brine interactions and the effects of core handling on wettability. J. Pet. Technol. U. S. 38, 11. https://doi.org/10.2118/13932-PA.

Barclay, S.A., Worden, R.H., 2000. Effects of reservoir wettability on quartz cementation in oil fields. In: Quartz Cementation in Sandstones. John Wiley & Sons, Ltd, pp. 103–117. https://doi.org/10.1002/9781444304237.ch8.

Brunauer, S., Emmett, P.H., Teller, E., 1938. Adsorption of gases in multimolecular layers. J. Am. Chem. Soc. 60, 309–319. https://doi.org/10.1021/ja01269a023.

Butler, J.P., Reeds, J.A., Dawson, S.V., 1981. Estimating solutions of first kind integral equations with nonnegative constraints and optimal smoothing. SIAM J. Numer. Anal. 18, 381–397. https://doi.org/10.1137/0718025.

Cao, Z., Gao, J., Liu, G., Zhang, J., Kong, Y., Yue, B., 2017. Investigation of oil potential in saline lacustrine shale, a case study of the Middle Permian Pingdiquan shale (Lucaogou equivalent) in the Junggar Basin, northwest China. Energy Fuels 31 (7), 6670–6688. https://doi.org/10.1021/acs.energyfuels.7b00294.

Cudjoe, S., Vinassa, M., Henrique Bessa Gomes, J., Barati, R.G., 2016. A comprehensive approach to sweet-spot mapping for hydraulic fracturing and CO_2 huff-n-puff injection in Chattanooga shale formation. J. Nat. Gas Sci. Eng. 33, 1201–1218. https://doi.org/10.1016/j.jngse.2016.03.042.

EIA, 2021. Annual Energy Outlook 2021 with Projections to 2050 [WWW Document]. URL. https://www.eia.gov/outlooks/aeo/pdf/00%20AEO2021%20Chart%20Library.pdf. (Accessed 6 November 2022).

Fleury, M., Gautier, S., Norrant, F., Kohler, E., 2011. Characterization of Nanoporous Systems with Low Field Nmr: Application to Kaolinite and Smectite Clays. Presented at the International Symposium of the Society of Core Analysts, Austin, Texas, USA, p. 12.

Fleury, M., Romero-Sarmiento, M., 2016. Characterization of shales using T1–T2 NMR maps. J. Pet. Sci. Eng. 137, 55–62. https://doi.org/10.1016/j.petrol.2015.11.006.

Gorynski, K.E., Tobey, M.H., Enriquez, D.A., Smagala, T.M., Dreger, J.L., Newhart, R.E., 2019. Quantification and characterization of hydrocarbon-filled porosity in oil-rich shales using integrated thermal extraction, pyrolysis, and solvent extraction. AAPG Bull. 103, 723–744. https://doi.org/10.1306/08161817214.

Guan, M., Liu, X., Jin, Z., Lai, J., Liu, J., Sun, B., Liu, T., Hua, Z., Xu, W., Shu, H., Wang, G., Liu, M., Luo, Y., 2022. Quantitative characterization of various oil contents and spatial distribution in lacustrine shales: insight from petroleum compositional characteristics derived from programed pyrolysis. Mar. Petrol. Geol. 138, 105522. https://doi.org/10.1016/j.marpetgeo.2021.105522.

Han, Y., Horsfield, B., Mahlstedt, N., Wirth, R., Curry, D.J., LaReau, H., 2019. Factors controlling source and reservoir characteristics in the Niobrara shale oil system, Denver Basin. AAPG Bull. 103, 2045–2072. https://doi.org/10.1306/0121191619717287.

Han, Y., Mahlstedt, N., Horsfield, B., 2015. The Barnett Shale: compositional fractionation associated with intraformational petroleum migration, retention, and expulsion. AAPG Bull. 99, 2173–2202. https://doi.org/10.1306/06231514113.

Hruljova, J., Savest, N., Oja, V., Suuberg, E.M., 2013. Kukersite oil shale kerogen solvent swelling in binary mixtures. Fuel 105, 77–82. https://doi.org/10.1016/j.fuel.2012.06.085.

Hu, T., Pang, X., Jiang, F., Wang, Q., Liu, X., Wang, Z., Jiang, S., Wu, G., Li, C., Xu, T., Li, M., Yu, J., Zhang, C., 2021. Movable oil content evaluation of lacustrine organic-rich shales: methods and a novel quantitative evaluation model. Earth Sci. Rev. 214, 103545. https://doi.org/10.1016/j.earscirev.2021.103545.

Huang, L., Khoshnood, A., Firoozabadi, A., 2020. Swelling of Kimmeridge kerogen by normal-alkanes, naphthenes and aromatics. Fuel 267, 117155. https://doi.org/10.1016/j.fuel.2020.117155.

Janssen, C., Wirth, R., Reinicke, A., Rybacki, E., Naumann, R., Wenk, H.R., Dresen, G., 2011. Nanoscale porosity in SAFOD core samples (san andreas fault). Earth Planet Sci. Lett. 301, 179–189. https://doi.org/10.1016/j.epsl.2010.10.040.

Jarvie, D.M., 2012. Shale resource systems for oil and gasPart 2—shale-oil resource systems. In: Shale Reservoirs—Giant Resources for the 21st Century. American Association of Petroleum Geologists. https://doi.org/10.1306/13321447M973489.

Jarvie, D.M., 2014. Components and processes affecting producibility and commerciality of shale resource systems. Geologica Acta 12, 307–325. https://doi.org/10.1344/GEOLOGICAACTA2014.12.4.3.

Jiang, C., Chen, Z., Mort, A., Milovic, M., Robinson, R., Stewart, R., Lavoie, D., 2016. Hydrocarbon evaporative loss from shale core samples as revealed by Rock-Eval and thermal desorption-gas chromatography analysis: its geochemical and geological implications. Mar. Petrol. Geol. 70, 294–303. https://doi.org/10.1016/j.marpetgeo.2015.11.021.

Jiang, Y., Xu, G., Bi, H., Shi, Y., Gao, Y., Han, X., Zeng, X., 2021. A new method to determine surface relaxivity of tight sandstone cores based on LF-NMR and high-speed centrifugation measurements. J. Pet. Sci. Eng. 196, 108096. https://doi.org/10.1016/j.petrol.2020.108096.

Jin, Z., Liang, X., Bai, Z., 2022. Exploration breakthrough and its significance of Gulong lacustrine shale oil in the Songliao Basin, Northeastern China. Energy Geosci 3, 120–125. https://doi.org/10.1016/j.engeos.2022.01.005.

Karimi, S., Saidian, M., Prasad, M., Kazemi, H., 2015. Reservoir rock characterization using centrifuge and nuclear magnetic resonance: a laboratory study of middle bakken cores. In: Presented at the SPE Annual Technical Conference and Exhibition, OnePetro. https://doi.org/10.2118/175069-MS.

Katz, B., Lin, F., 2014. Lacustrine basin unconventional resource plays: key differences. Mar. Petrol. Geol. 56, 255–265. https://doi.org/10.1016/j.marpetgeo.2014.02.013.

Kennedy, M.J., Pevear, D.R., Hill, R.J., 2002. Mineral surface control of organic carbon in black shale. Science 295, 657–660. https://doi.org/10.1126/science.1066611.

Khatibi, S., Ostadhassan, M., Xie, Z., Gentzis, T., Bubach, B., Gan, Z., Carvajal-Ortiz, H., 2019. NMR relaxometry a new approach to detect geochemical properties of organic matter in tight shales. Fuel 235, 167–177. https://doi.org/10.1016/j.fuel.2018.07.100.

Kuila, U., Prasad, M., 2013. Specific surface area and pore-size distribution in clays and shales. Geophys. Prospect. 61, 341–362. https://doi.org/10.1111/1365-2478.12028.

Lei, Q., Xu, Y., Cai, B., Guan, B., Wang, X., Bi, G., Li, H., Li, S., Ding, B., Fu, H., Tong, Z., Li, T., Zhang, H., 2022. Progress and prospects of horizontal well fracturing technology for shale oil and gas reservoirs. Petrol. Explor. Dev. 49, 191–199. https://doi.org/10.1016/S1876-3804(22)60015-6.

Li, J., Huang, W., Lu, S., Wang, M., Chen, G., Tian, W., Guo, Z., 2018. Nuclear magnetic resonance T1–T2 map division method for hydrogen-bearing components in continental shale. Energy Fuels. https://doi.org/10.1021/acs.energyfuels.8b01541.

Li, J., Jiang, C., Wang, M., Lu, S., Chen, Z., Chen, G., Li, J., Li, Z., Lu, S., 2020a. Adsorbed and free hydrocarbons in unconventional shale reservoir: a new insight from NMR T1-T2 maps. Mar. Petrol. Geol. 116, 104311. https://doi.org/10.1016/j.marpetgeo.2020.104311.

Li, T., Huang, Z., Feng, Y., Chen, X., Ma, Q., Liu, B., Guo, X., 2020b. Reservoir characteristics and evaluation of fluid mobility in organic-rich mixed siliciclastic-carbonate sediments: a case study of the lacustrine Qiketai Formation in Shengbei Sag, Turpan-Hami Basin, Northwest China. J. Pet. Sci. Eng. 185, 106667. https://doi.org/10.1016/j.petrol.2019.106667.

Liu, B., Bai, L., Chi, Y., Jia, R., Fu, X., Yang, L., 2019. Geochemical characterization and quantitative evaluation of shale oil reservoir by two-dimensional nuclear magnetic resonance and quantitative grain fluorescence on extract: a case study from the Qingshankou Formation in Southern Songliao Basin, northeast China. Mar. Petrol. Geol. 109, 561–573. https://doi.org/10.1016/j.marpetgeo.2019.06.046.

Liu, B., Jiang, X., Bai, L., Lu, R., 2021a. Investigation of oil and water migrations in lacustrine oil shales using 20 MHz 2D NMR relaxometry techniques. Petrol. Sci. https://doi.org/10.1016/j.petsci.2021.10.011.

Liu, C., Xu, X., Liu, K., Bai, J., Liu, W., Chen, S., 2020a. Pore-scale oil distribution in shales of the Qingshankou Formation in the changling sag, Songliao Basin, NE China. Mar. Petrol. Geol. 120, 104553. https://doi.org/10.1016/j.marpetgeo.2020.104553.

Liu, Y., Zeng, J., Yang, G., Jia, W., Liu, S., Kong, X., Li, S., 2021b. An innovative method for the characterization of oil content in lacustrine shale-oil systems: a case study from the Middle Permian Lucaogou Formation in the Jimusaer Sag, Junggar Basin. Mar. Petrol. Geol. 130, 105112. https://doi.org/10.1016/j.marpetgeo.2021.105112.

Liu, Z., Liu, D., Cai, Y., Yao, Y., Pan, Z., Zhou, Y., 2020b. Application of nuclear magnetic resonance (NMR) in coalbed methane and shale reservoirs: a review. Int. J. Coal Geol. 218, 103261. https://doi.org/10.1016/j.coal.2019.103261.

Mayer, L.M., 1994. Relationships between mineral surfaces and organic carbon concentrations in soils and sediments. Chem. Geol. 114, 347–363. https://doi.org/10.1016/0009-2541(94)90063-9.

Mehana, M., El-monier, I., 2016. Shale characteristics impact on Nuclear Magnetic Resonance (NMR) fluid typing methods and correlations. Petroleum 2, 138–147. https://doi.org/10.1016/j.petlm.2016.02.002.

Nicot, B., Vorapalawut, N., Rousseau, B., Madariaga, L.F., Hamon, G., Korb, J.-P., 2016. Estimating saturations in organic shales using 2D NMR. Petrophysics - SPWLA J. Form. Eval. Reserv. Descr. 57, 19–29.

Pepper, A.S., Corvi, P.J., 1995. Simple kinetic models of petroleum formation. Part III: modelling an open system. Mar. Petrol. Geol. 12, 417–452. https://doi.org/10.1016/0264-8172(95)96904-5.

Robin, M., Rosenberg, E., Fassi-Fihri, O., 1995. Wettability studies at the pore level: a new approach by use of cryo-SEM. Spe form. Evaluation 10, 11–19. https://doi.org/10.2118/22596-PA.

Romero-Sarmiento, M.F., 2019. A quick analytical approach to estimate both free versus sorbed hydrocarbon contents in liquid-rich source rocks. AAPG Bull. 103, 2031–2043. https://doi.org/10.1306/02151918152.

Sang, G., Liu, S., Zhang, R., Elsworth, D., He, L., 2018a. Nanopore characterization of

mine roof shales by SANS, nitrogen adsorption, and mercury intrusion: impact on water adsorption/retention behavior. Int. J. Coal Geol. 200, 173–185. https://doi.org/10.1016/j.coal.2018.11.009.
Sang, Q., Zhang, S., Li, Y., Dong, M., Bryant, S., 2018b. Determination of organic and inorganic hydrocarbon saturations and effective porosities in shale using vacuum-imbibition method. Int. J. Coal Geol. 200, 123–134. https://doi.org/10.1016/j.coal.2018.10.010.
Schmitt, M., Fernandes, C.P., da Cunha Neto, J.A.B., Wolf, F.G., dos Santos, V.S.S., 2013. Characterization of pore systems in seal rocks using nitrogen gas adsorption combined with mercury injection capillary pressure techniques. Mar. Petrol. Geol. 39, 138–149. https://doi.org/10.1016/j.marpetgeo.2012.09.001.
Silletta, E.V., Vila, G.S., Domené, E.A., Velasco, M.I., Bedini, P.C., Garro-Linck, Y., Masiero, D., Monti, G.A., Acosta, R.H., 2022. Organic matter detection in shale reservoirs using a novel pulse sequence for T1-T2 relaxation maps at 2 MHz. Fuel 312, 122863. https://doi.org/10.1016/j.fuel.2021.122863.
Sing, K.S.W., 1985. Reporting physisorption data for gas/solid systems with special reference to the determination of surface area and porosity (Recommendations 1984). Pure Appl. Chem. 57, 603–619. https://doi.org/10.1351/pac198557040603.
Soeder, D.J., 2018. The successful development of gas and oil resources from shales in North America. J. Pet. Sci. Eng. 163, 399–420. https://doi.org/10.1016/j.petrol.2017.12.084.
Sun, L., Liu, H., He, W., Li, G., Zhang, S., Zhu, R., Jin, X., Meng, S., Jiang, H., 2021. An analysis of major scientific problems and research paths of Gulong shale oil in Daqing Oilfield, NE China. Petrol. Explor. Dev. 48, 527–540. https://doi.org/10.1016/S1876-3804(21)60043-5.
Tang, H., Wang, J., Zhang, L., Guo, J., Chen, H., Liu, J., Pang, M., Feng, Y., 2016. Testing method and controlling factors of specific surface area of shales. J. Pet. Sci. Eng. 143, 1–7. https://doi.org/10.1016/j.petrol.2016.02.009.
Tian, S., Xue, H., Lu, S., Zeng, F., Xue, Q., Chen, G., Wu, C., Zhang, S., 2017. Molecular simulation of oil mixture adsorption character in shale system. J. Nanosci. Nanotechnol. 17, 6198–6209. https://doi.org/10.1166/jnn.2017.14487.
Tissot, B.P., Welte, D.H., 1984. Petroleum Formation and Occurrence, second ed. Springer, Berlin, Heidelberg. https://doi.org/10.1007/978-3-642-87813-8.
Tran, T., Sinurat, P., Wattenbarger, R.A., 2011. Production Characteristics of the Bakken Shale Oil. In: Presented at the SPE Annual Technical Conference and Exhibition, OnePetro. https://doi.org/10.2118/145684-MS.
Wang, M., Li, M., Li, J.B., Xu, L., Zhang, J.Y., Zhang, J.X., 2022. The key parameter of shale oil resource evaluation: oil content. Petrol. Sci. https://doi.org/10.1016/j.petsci.2022.03.006.
Wang, M., Ma, R., Li, J., Lu, S., Li, C., Guo, Z., Li, Z., 2019. Occurrence mechanism of lacustrine shale oil in the Paleogene Shahejie Formation of Jiyang depression, Bohai Bay Basin, China. Petrol. Explor. Dev. 46, 833–846. https://doi.org/10.1016/S1876-3804(19)60242-9.
Wang, S., Javadpour, F., Feng, Q., 2016. Molecular dynamics simulations of oil transport through inorganic nanopores in shale. Fuel 171, 74–86. https://doi.org/10.1016/j.fuel.2015.12.071.
Washburn, K.E., Birdwell, J.E., 2013. Updated methodology for nuclear magnetic resonance characterization of shales. J. Magn. Reson. 233, 17–28. https://doi.org/10.1016/j.jmr.2013.04.014.
Washburn, K.E., Cheng, Y., 2017. Detection of intermolecular homonuclear dipolar coupling in organic rich shale by transverse relaxation exchange. J. Magn. Reson. 278, 18–24. https://doi.org/10.1016/j.jmr.2017.02.022.
Wu, S., Zhu, R., Yang, Z., Mao, Z., Cui, J., Zhang, X., 2019. Distribution and characteristics of lacustrine tight oil reservoirs in China. J. Asian Earth Sci. 178, 20–36. https://doi.org/10.1016/j.jseaes.2018.05.013.
Xu, Y., Lun, Z., Pan, Z., Wang, H., Zhou, X., Zhao, C., Zhang, D., 2022. Occurrence space and state of shale oil: a review. J. Pet. Sci. Eng. 211, 110183. https://doi.org/10.1016/j.petrol.2022.110183.
Yan, W., Sun, J., Cheng, Z., Li, J., Sun, Y., Shao, W., Shao, Y., 2017. Petrophysical characterization of tight oil formations using 1D and 2D NMR. Fuel 206, 89–98. https://doi.org/10.1016/j.fuel.2017.05.098.
Zeng, H., Huo, Q., Zhang, X., Fan, Q., Wang, Y., Lu, R., Pang, L., 2022. Quantitative analysis on occurrence evolution of Gulong shale oil in Songliao Basin. Pet. Geol. Oilfield Dev. Daqing 41, 80–90. https://doi.org/10.19597/J.ISSN.1000-3754.202111089.
Zhang, H., Huang, H., Li, Z., Liu, M., 2019. Oil physical status in lacustrine shale reservoirs – a case study on Eocene Shahejie Formation shales, Dongying Depression, East China. Fuel 257, 116027. https://doi.org/10.1016/j.fuel.2019.116027.
Zhang, J., Liu, G., Torsaeter, O., Tao, S., Jiang, M., Li, G., Zhang, S., 2020a. Pore-throat structure characteristics and its effect on flow behavior in Gaotaizi tight siltstone reservoir, northern Songliao Basin. Mar. Petrol. Geol. 122, 104651. https://doi.org/10.1016/j.marpetgeo.2020.104651.
Zhang, P., Lu, S., Li, J., Chang, X., 2020b. 1D and 2D Nuclear magnetic resonance (NMR) relaxation behaviors of protons in clay, kerogen and oil-bearing shale rocks. Mar. Petrol. Geol. 114, 104210. https://doi.org/10.1016/j.marpetgeo.2019.104210.
Zhang, T., Ellis, G.S., Ruppel, S.C., Milliken, K., Yang, R., 2012. Effect of organic-matter type and thermal maturity on methane adsorption in shale-gas systems. Org. Geochem. 47, 120–131. https://doi.org/10.1016/j.orggeochem.2012.03.012.
Zhao, X., Zhou, L., Pu, X., Jin, F., Han, W., Shi, Z., Chen, C., Jiang, W., Guan, Q., Xu, J., Liu, X., Zhang, W., Ma, J., 2022. Theories, technologies and practices of lacustrine shale oil exploration and development: a case study of Paleogene Kongdian Formation in Cangdong sag, Bohai Bay Basin, China. Petrol. Explor. Dev. 49, 707–718. https://doi.org/10.1016/S1876-3804(22)60059-4.
Zhao, Z., Littke, R., Zieger, L., Hou, D., Froidl, F., 2020. Depositional environment, thermal maturity and shale oil potential of the Cretaceous Qingshankou Formation in the eastern Changling Sag, Songliao Basin, China: an integrated organic and inorganic geochemistry approach. Int. J. Coal Geol. 232, 103621. https://doi.org/10.1016/j.coal.2020.103621.
Zhu, C., Guo, W., Li, Y., Gong, H., Sheng, J.J., Dong, M., 2021. Effect of occurrence states of fluid and pore structures on shale oil movability. Fuel 288, 119847. https://doi.org/10.1016/j.fuel.2020.119847.
Zhu, X., Cai, J., Xu, X., Xie, Z., 2013. Discussion on the method for determining BET specific surface area in argillaceous source rocks. Mar. Petrol. Geol. 48, 124–129. https://doi.org/10.1016/j.marpetgeo.2013.08.003.